

THESIS FOR THE DEGREE OF LICENTIATE OF ENGINEERING

**Towards graphene-based devices: Fabrication and
characterization**

NICLAS LINDVALL



**Department of Microtechnology and Nanoscience
CHALMERS UNIVERSITY OF TECHNOLOGY
Gothenburg, Sweden 2012**

Towards graphene-based devices: Fabrication and characterization
NICLAS LINDVALL

© NICLAS LINDVALL, 2012

Chalmers University of Technology
Microtechnology and Nanoscience (MC2)
Quantum Device Physics Laboratory
SE-412 96 Gothenburg, Sweden
Phone: +46 (0)31-772 1000

ISSN 1652-0769
Technical report MC2-230

Chalmers Reproservice
Gothenburg Sweden 2012

Towards graphene-based devices: Fabrication and characterization

NICLAS LINDVALL

Department of Microtechnology and Nanoscience (MC2)

Chalmers University of Technology

Gothenburg, Sweden 2012

Abstract

Graphene is a new material with a large set of impressive properties, interesting both for fundamental studies and applications. Reliable synthesis of large-scale, high-quality graphene is key to its future success. This thesis is focused on the development of such fabrication techniques and experimental studies on three different graphene-based devices.

The highest quality graphene is produced by mechanical exfoliation of graphite. While this technique is not scalable, it provides high quality graphene for scientific purposes and proof of principle devices. Catalytic chemical vapor deposition of graphene on copper is the most promising scalable method for graphene synthesis. Techniques for high temperature growth of graphene from methane as a precursor gas on high-purity copper foils are developed. Also, techniques for transferring the as-grown graphene to insulating substrates are presented. Large-scale graphene with high uniformity and a mobility $\sim 3000 \text{ cm}^2/\text{Vs}$ at room temperature is obtained.

The transfer process needed for catalytically grown graphene on copper introduces issues with process reliability and future integration in semiconductor manufacturing. A non-catalytic chemical vapor deposition technique is shown to give uniform large-area graphene directly on insulating substrates like SiO_2 and Si_3N_4 , avoiding transfer. Raman spectroscopy, transmission electron microscopy, and transport measurements show that graphene grown this way is nanocrystalline and its electronic properties are inferior to those of catalytically grown graphene.

Contamination and unintentional doping are difficult to avoid in graphene processing. A mechanical cleaning technique using an atomic force microscope is shown to efficiently remove contaminants and improve the electronic properties of graphene. The technique is easy and can be applied to substrates that cannot sustain standard graphene cleaning procedures.

Graphene devices are realized on ferroelectric barium strontium titanate. The strong field effect in graphene is utilized as a read-out of the ferroelectric state, thus realizing a hybrid graphene-ferroelectric memory device.

A graphene-based cold-electron bolometer is fabricated and characterized at cryogenic temperature. The low volume of graphene makes it an interesting absorber material for high-sensitivity bolometers.

The Aharonov-Bohm effect is studied in graphene rings having metallic mirrors. The mirrors confine electrons to the Aharonov-Bohm ring, improving the visibility of higher-order Aharonov-Bohm oscillations.

Keywords: Graphene, Chemical vapor deposition, Synthesis, Mechanical cleaning, Ferroelectric, Bolometer, Aharonov-Bohm effect

This thesis is based partly on the following scientific papers:

I. J. Sun, N. Lindvall, M. Cole, K. Angel, T. Wang, K. Teo, D. Chua, J. Liu, and A. Yurgens, "Low partial pressure chemical vapor deposition of graphene on copper", *IEEE Trans Nanotechnol* vol. **11**, pp 255-260, 2012.

II. J. Sun, N. Lindvall, M. T. Cole, T. Wang, T. J. Booth, P. Boggild, K. B. K. Teo, J. Liu, and A. Yurgens, "Controllable chemical vapor deposition of large area uniform nanocrystalline graphene directly on silicon dioxide", *J Appl Phys* vol. **111**, p. 044103, 2012.

III. J. Sun, M. T. Cole, N. Lindvall, K. B. K. Teo, and A. Yurgens, "Noncatalytic chemical vapor deposition of graphene on high-temperature substrates for transparent electrodes", *Appl Phys Lett* vol. **100**, p. 022102, 2012.

IV. J. Sun, N. Lindvall, M. T. Cole, K. B. K. Teo, and A. Yurgens, "Large-area uniform graphene-like thin films grown by chemical vapor deposition directly on silicon nitride", *Appl Phys Lett* vol. **98**, p. 252107, 2011.

V. N. Lindvall, A. Kalabukhov, and A. Yurgens, "Cleaning graphene using atomic force microscope", *J Appl Phys* vol. **111**, pp 064904-064904, 2012.

VI. M. Tarasov, N. Lindvall, L. Kuzmin, and A. Yurgens, "Family of graphene-based superconducting devices", *JETP Lett* vol. **94**, pp 329-332, 2011.

VII. Y. Nam, J. S. Yoo, Y. W. Park, N. Lindvall, T. Bauch, and A. Yurgens, "The Aharonov-Bohm effect in graphene with metal mirrors", submitted to *Carbon*.

The contribution by the author of this thesis, Niclas Lindvall, to these papers was as follows:

I. JS, TW, and I did the sample fabrication. JS, AY, and I did electrical characterization. MC and KT did Raman measurements. KA and DC did TEM characterization. JS wrote the paper with input from the co-authors.

II. JS, TW, and I did the sample fabrication and developed the technique. JS, MC, TB, PB, KT, AY, and I did the characterization and measurements. JS wrote the manuscript and completed the submission with the help of the co-authors.

III. JS and I did the sample fabrication. JS, MC, KT, and I did sample characterization and measurements. JS wrote the manuscript and completed the submission with the help of the co-authors.

IV. JS and I did sample fabrication. MC and KT provided Raman characterization. JS, AY, and I did the electrical characterization. JS wrote the paper and completed the submission procedure with the help of the other co-authors.

V. I was responsible for the idea behind the paper. AK and I worked on sample fabrication. I was responsible also for measurements and data analysis. AY gave input on the data analysis. I wrote the first draft of the paper. After input from the co-authors, I finalized the manuscript and completed the submission procedure.

VI. I did the sample fabrication and process development. MT and I did the measurements. MT wrote the paper.

VII. YN, JY, and I did the sample fabrication. YN, TB, AY, and I performed the measurements. YN wrote the paper.

Other scientific papers of the author that are outside the scope of this thesis:

VIII. Y. Fu, B. Carlberg, N. Lindahl, N. Lindvall, J. Bielecki, A. Matic, Y. Song, Z. Hu, Z. Lai, L. Ye, J. Sun, Y. Zhang, Y. Zhang, and J. Liu, "Templated Growth of Covalently Bonded Three-Dimensional Carbon Nanotube Networks Originated from Graphene", *Adv Mater* vol. **24**, pp 1576-1581, 2012.

IX. Y. Nam, N. Lindvall, J. Sun, Y. W. Park, and A. Yurgens, "Graphene p–n–p junctions controlled by local gates made of naturally oxidized thin aluminium films", *Carbon* vol. **50**, pp 1987-1992, 2012.

X. J. Svensson, N. Lindahl, H. Yun, M. Seo, D. Midtvedt, Y. Tarakanov, N. Lindvall, O. Nerushev, J. Kinaret, S. Lee, and E. E. B. Campbell, "Carbon nanotube field effect transistors with suspended graphene gates", *Nano Lett* vol. **11**, pp 3569-3575, 2011.

XI. J. Sun, M. T. Cole, S. A. Ahmad, O. Bäcke, T. Ive, M. Löffler, N. Lindvall, E. Olsson, K. B. K. Teo, J. Liu, A. Larsson, A. Yurgens, and Å. Haglund, "Direct chemical vapor deposition of large-area carbon thin films on gallium nitride for transparent electrodes: A first attempt", accepted for publication in *IEEE Trans Semicond Manuf*.

List of symbols

a	loop area
A	overlapping area of graphene and gate electrode
\mathbf{A}	magnetic vector potential
B	magnetic flux density
C	cantilever spring constant
C_g	specific gate capacitance
d	thickness of dielectric
e	elementary charge
E	energy of charge carriers
E_F	Fermi energy
g_s	degeneracy factor
k, k_x, k_y	wave vector components for charge carriers
l	integer index
l_ϕ	phase coherence length
m	mass of charge carriers
n	charge carrier concentration
n_g	charge carrier concentration induced by gate
n_i	refractive index of material layer i
n_0	residual charge carrier concentration
N	index of Aharonov-Bohm oscillations
N_{sq}	number of geometrical squares
I	electrical current
I_D	Raman intensity of D peak
I_G	Raman intensity of G peak
I_{op}	optical intensity
r	relative index of refraction
R	electrical resistance
R_H	Hall coefficient
R_{RMS}	height root mean square
R_{xx}	longitudinal resistance
R_{xy}	transversal resistance
$R_{contact}$	contact resistance
q	individual carrier charge
V_D	Dirac voltage
V_g	gate voltage
V_{xy}	transversal voltage
V_{xx}	longitudinal voltage
ϵ_r	relative permittivity
λ	optical wavelength
μ	charge carrier mobility
$\tilde{\mu}$	approximate charge carrier mobility
ρ_{xx}	longitudinal resistivity
ρ_{xy}	Hall resistivity
σ	electrical conductance
v_F	Fermi velocity
ϕ	charge carrier phase
Φ	optical phase shift

List of abbreviations

AFM	atomic force microscopy
BSTO	barium strontium titanate
CEB	cold-electron bolometer
CNT	carbon nanotube
CVD	chemical vapor deposition
DOS	density of states
FFT	fast Fourier transform
HE	Hall effect
ICT	information and communications technology
IQHE	integer quantum Hall effect
NEMS	nanoelectromechanical systems
RMS	root mean square
PMMA	polymethyl-methacrylate
PZT	lead zirconate titanate, $\text{Pb}(\text{Zr}_{0.2}\text{Ti}_{0.8})\text{O}_3$
SEM	scanning electron microscopy
SIN	superconductor-insulator-normal metal
STO	strontium titanate
TEM	transmission electron microscopy
UCFs	universal conductance fluctuations

Contents

List of publications	V
Symbols	VIII
Abbreviations	IX
Contents	XI
1 Introduction	1
1.1 Carbon wonder material	1
1.2 Aim and outline	5
2 Theory	7
2.1 Electronic properties	7
2.2 Field effect.....	8
2.3 Hall effect.....	10
2.4 Quantum Hall effect	11
2.5 Aharonov-Bohm effect.....	12
2.6 Optical visibility	13
3 Graphene fabrication	17
3.1 Mechanical exfoliation.....	17
3.2 Chemical vapor deposition on copper.....	18
3.3 Chemical vapor deposition on insulators.....	21
3.4 Substrate layout and nanofabrication.....	23
4 Material characterization	27
4.1 Graphene produced by mechanical exfoliation.....	27

4.2	Graphene produced by catalytic CVD.....	30
4.3	Graphene produced by non-catalytic CVD.....	32
5	Cleaning using atomic force microscope	37
5.1	Introduction.....	37
5.2	Experiment and results.....	38
5.3	Conclusions.....	41
6	Graphene on ferroelectrics	43
6.1	Introduction.....	43
6.2	Experiment and results.....	43
6.3	Conclusions.....	45
7	Graphene bolometer	47
7.1	Introduction.....	47
7.2	Experiment and results.....	47
7.3	Conclusions.....	49
8	Aharonov-Bohm effect in graphene	51
8.1	Introduction.....	51
8.2	Experiment and results.....	52
8.3	Conclusions.....	54
	Appendix A: Recipes for sample fabrication	55
	Acknowledgements	57
	Bibliography	59
	Appended papers	69

1 Introduction

New technology is both a catalyzer and a driving force for the development of our society, historically as well as in modern times. The key components of a new technology are new materials. From the stone-, bronze-, and iron ages, where the material name even followed them into the history books, to modern times with polymers (plastics) and silicon (transistors, electronics), the civilization of that time has been significantly affected by a single technology. At our present time, we are in the information and communications technology (ICT) era awaiting, as always, the next big technological breakthrough.

While technological revolutions are inherently difficult, if not impossible, to predict, we can identify some key technological challenges for the near future. These include several energy-related problems such as the never-ending increasing need for more of it while reducing its environmental impact, and new types of energy storage systems i.e. better batteries or supercapacitors. We crave for faster, more clever, and more power-efficient electronics, possibly making them flexible and transparent. For these challenges, new materials are needed.

While many materials may share one or maybe two of the properties needed for such future applications, for a material to be truly revolutionary it will need to incorporate many. This thesis is about such a material, graphene, which is hoped to play a role in not one but all of the above mentioned applications, as well as in many others.

Graphene will be introduced with an overview of its properties and potential applications in Chapter 1.1. In Chapter 1.2, the aim and outline of this thesis are presented.

1.1 Carbon wonder material

Carbon is one of the most versatile and important materials on earth. It is the building block for (almost) all life, the base for the field of organic chemistry, and has in different forms provided great historic importance. Its versatility and usefulness is largely thanks to the many different ways the four valence electrons of carbon can form chemical bonds. Two of the valence electrons are in s orbitals and two in p orbitals. These orbitals can hybridize, meaning that one s electron is promoted to a p orbital while one (sp^1 -hybridization), two (sp^2 -hybridization), or three (sp^3 -

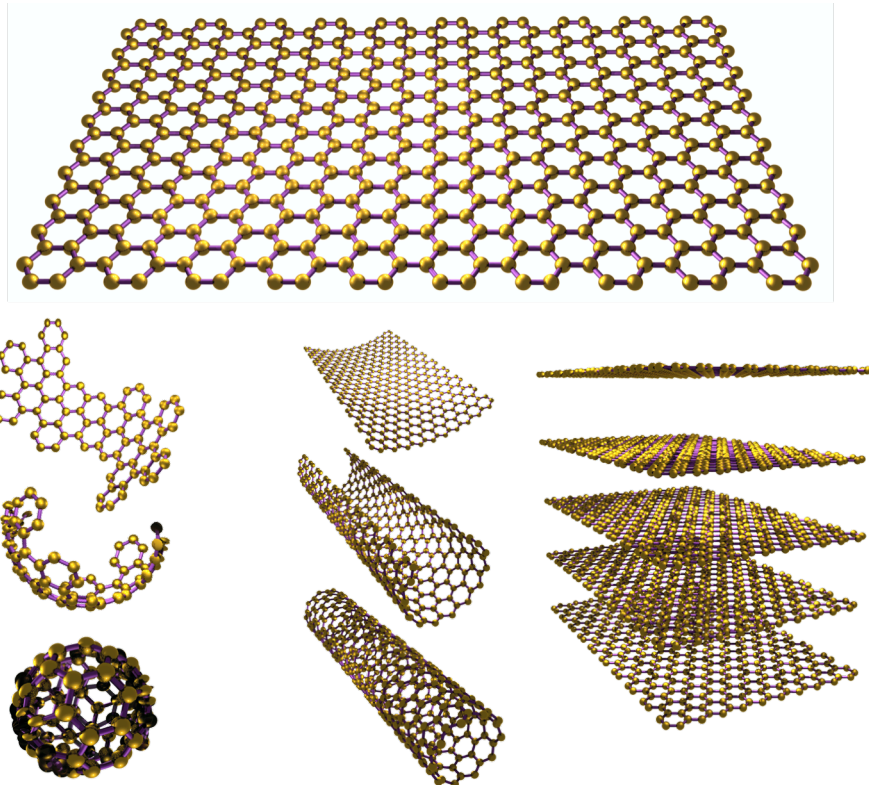


Figure 1.1: Graphene (top) is a hexagonal honeycomb lattice of sp^2 -hybridized carbon atoms. It can be viewed as the 2D building block for the other sp^2 -hybridized carbon allotropes. These are the fullerene (0D, bottom left), the carbon nanotube (1D, bottom center), and graphite (3D, bottom right).

hybridization) of the p orbitals mix with the other s orbital. In the case of sp^3 -hybridization, all four valence electrons form σ bonds. These are strong bonds with localized electrons, yielding for example diamond, which is among the hardest materials that exist and is electrically insulating. In the case of sp^2 -hybridized carbon, three valence electrons form σ bonds while the fourth is in the π orbital. This electron is not localized and contributes to the electrical conductivity of sp^2 -hybridized carbon materials.

Graphene is a one atom thick hexagonal lattice of carbon atoms. It is the two-dimensional (2D) allotrope of sp^2 -hybridized carbon. It is a single layer of graphite and can be viewed as the building block for the other sp^2 -hybridized carbon allotropes. The three other allotropes, covering a range of dimensionality, are seen in Figure 1.1: the fullerene (zero-dimensional, 0D), the carbon nanotube (CNT, one-dimensional, 1D), and graphite (three-dimensional, 3D). Graphene shares several of its properties with the others, especially with CNTs. The strong σ bonds are responsible for the mechanical properties and the inertness of the materials, while the π electron can move freely and gives rise to the high electrical conductivity.

While several works from the 1970s and later have reported on the formation of atomically thin layers of graphite on silicon carbide [1] and metal substrates [2], it was not until 2004 and 2005 that such layers were sufficiently decoupled from their

environment to manifest their distinct properties [3-5]. For this achievement, Andre Geim and Konstantin Novoselov were awarded the Nobel Prize in Physics 2010.

It was long argued that a strictly 2D crystal could not exist at any finite temperature because thermal fluctuations would lead to unsustainable atomic displacements [6-8]. Monolayers could only be found as parts of 3D structures. However, with the experiments on the graphitic monolayer graphene, it was shown that 2D crystals could indeed exist on non-crystalline support substrates, clamped suspended between support points, and in liquid suspension [3, 4].

What makes graphene extraordinary, justifying the huge amount of resources spent on it [9], is not the impressive properties and superlatives it inherits per se. It is the fact that it inherits so many of them. It is the first truly two-dimensional material, being only one atom thick (the π orbitals span approximately 0.34 nm). This leads to a specific surface area of $\sim 2600 \text{ m}^2/\text{g}$ [10]. While being atomically thin, it is still impermeable, even to helium [11]. It is the strongest material ever measured with a Young's modulus of $\sim 1 \text{ TPa}$ while being stretchable up to 25 % [12]. Its charge carriers have zero effective mass (imitating the behavior of massless Dirac fermions) and exhibit a mobility exceeding $10^6 \text{ cm}^2/\text{Vs}$ [13]. Graphene shows the record thermal conductivity of $\sim 5000 \text{ W/mK}$ [14]. It is also almost transparent (it absorbs $\sim 2.3 \%$ of any visible wavelength) [15] but is still an interesting material for photonic applications [16, 17].

Such exotic properties pave grounds for fundamental studies in Chemistry and Physics, but also for an increasing number of technical applications. The most

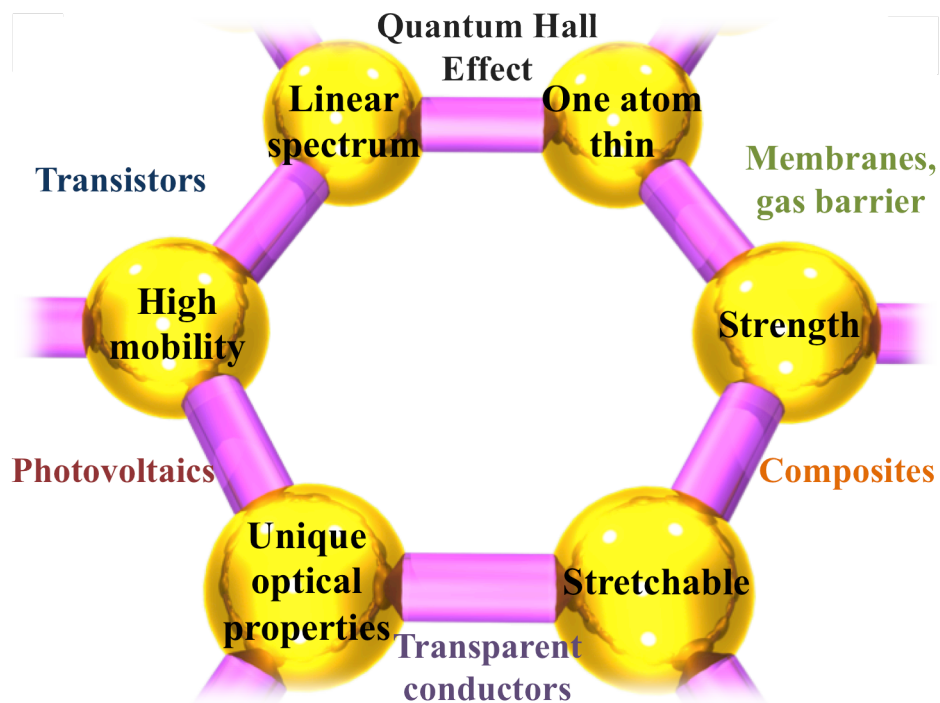


Figure 1.2: Hexagonal view of six of the most exciting properties of graphene and six promising fields of applications. Each application field combines at least two of those properties. Many applications incorporate more than two particular properties.

interesting applications combine several of these properties. Figure 1.2 shows six different application fields, each based on at least two distinct properties of graphene. Graphene can be used as a new, more accurate, resistance standard based on its unique version of the integer quantum Hall effect (IQHE). The combination of high mechanical strength and impermeability suggests promise for use as a gas barrier or suspended membrane in nanoelectromechanical systems (NEMS). Composite materials is another field where its mechanical strength can help improve performance while adding functionality by making the material both highly stretchable and electrically- and thermally conducting [18]. Probably, the most promising electronic application in short term is the use of graphene as a transparent and flexible electrode [19, 20]. Also, its optical and electronic properties could lead to improved photovoltaics and new kinds of sensors [21-24].

Previously, great hope was put in using graphene in high frequency transistors, both in digital logic- and analogue circuits. It is foreseen that silicon-based transistors in digital logic will eventually have to be replaced to enable the continuation of performance improvements following Moore's law [25, 26]. Hence, there is an intensive search for replacement materials. While high frequency operation up to 300 GHz has been shown for graphene transistors [27], and predictions estimate that it could be pushed to the THz range [28], the lack of a band gap makes it difficult to achieve a low leakage current in digital logics and a large power gain in analogue applications [29, 30]. Several ways to open a band gap in graphene exist, but so far it has not been possible to achieve a sizeable band gap while maintaining high charge carrier mobility. It is unclear if this is a fundamental limitation and whether we will ever see a carbon-based processor.

Not all electronics require extremely high carrier mobilities. Ink-jet printed electronics are low-cost devices for a variety of applications where a modest electronic performance is acceptable. Traditionally, the charge carrier mobility for this technology is less than $1 \text{ cm}^2/\text{Vs}$. Using graphene-based inks, the mobility can be as high as $\sim 95 \text{ cm}^2/\text{Vs}$, an improvement of two orders of magnitude. Graphene-based inks are the first commercially available products based on graphene.

Graphene may also find its place within several energy applications. It can be used as an electrode in batteries [31, 32], for fuel- and other electrochemical cells [33, 34], and in ultracapacitors [10].

Such a comprehensive list of potential applications has initiated a rush for immaterial property connected to graphene [35]. With fabrication methods rapidly improving, this might just be the beginning of the graphene gold rush. Three things are, however, worth noting. First, the Kroemer's lemma states that "*the principal applications of any sufficiently new and innovative technology have always been applications that were created by that technology, rather than being pre-existing applications, where the new technology simply provided improvements.*" [36]. That is, for the technology to succeed, it is likely to do so based on completely new applications.

Second, in the case of CNTs a lot of hype was initiated, promising revolutionary applications [37]. More than twenty years later, almost no applications have been

realized. There is, however, one distinct difference: Graphene is planar technology, which is much easier to implement in most fabrication processes. In this case, it can be compared to diamond-like carbon, which is planar carbon (mostly sp^3 -hybridized), and is used in great volumes in many applications [38, 39].

Third, there exist many different types of graphene depending on the method of fabrication and how it is integrated. These different types are essentially different materials with different properties and applications. Hence, it is more correct to talk about a graphene material family, rather than the single material. In this case, they do not all share the same strengths and weaknesses, making it more likely that at least some could succeed.

On several occasions throughout history, great technological breakthroughs have been accompanied by great health hazards. Since graphene is, as are many nanomaterials, a new material with hopes of use in many different applications, its potential health hazards are an important concern. While much focus is put on this issue, very little scientific work has been published and its environmental impact and potential health hazards remain largely unknown so far [40-42].

For a more detailed introduction to graphene, the review of Geim *et al.* [43] is recommended.

1.2 Aim and outline

The aim of this thesis is to describe different ways to produce graphene, characterize its properties, show how to clean it, and describe experiments showing its potential for future applications. The field of graphene research is still young and rapidly changing. Therefore, it is of a broad and fragmented nature, which is reflected by the many different topics covered in this thesis. A large emphasis is put on fabrication techniques, which are key for the development of graphene technology.

In Chapter 2, the theory of graphene is briefly presented. It is a short introduction useful for the understanding of subsequent chapters.

Chapter 3 describes the fabrication methods for graphene. In this thesis, graphene is produced by both cleavage of graphite and chemical vapor deposition. Graphene grown on copper (paper I) is first introduced. Then novel scalable fabrication techniques where graphene is grown directly on insulators are presented (papers II, III, and IV).

Characterization of the graphene is described in Chapter 4. Properties of graphene produced in different ways are obtained using electrical- and optical measurements, and electron microscopy.

In Chapter 5, a mechanical technique for cleaning graphene is presented (paper V).

Chapter 6 describes graphene devices on ferroelectric substrates which could be used in future memory devices.

Experiments on a graphene-based bolometer are presented in Chapter 7 (paper VI).

Finally, in Chapter 8 quantum transport measurements in graphene are shown. The Aharonov-Bohm effect is studied in a graphene nanostructure (paper **VII**).

2 Theory

Some key theoretical concepts needed for understanding the properties of graphene and the material characterization performed in later chapters are provided in this chapter. The electronic structure of graphene is presented in Chapter 2.1 and the field effect in Chapter 2.2. In Chapter 2.3, the Hall effect is described as a tool for characterizing graphene and in Chapter 2.4 the quantum Hall effect is introduced. The theory of the Aharonov-Bohm effect is presented in Chapter 2.5. How to engineer visibility of graphene on thin dielectrics is shown in Chapter 2.6.

2.1 Electronic properties

Maybe the single most remarkable graphene feature is its electronic properties [44]. Graphene is a zero band gap semimetal with a linear dispersion for low energy excitations. Figure 2.1 shows the dispersion relation for monolayer graphene. Close to the points where the conductance- and valence bands meet, the energy dispersion relation is linear in momentum. These, six per Brillouin zone, are denoted Dirac points. This is in contrast with free electrons and electrons in traditional semiconductor systems where the dispersion is quadratic:

$$E = \frac{\hbar}{2m} k^2 \propto \frac{1}{m} k^2, \quad (2.1)$$

where E is the energy, \hbar is the reduced Planck constant, m is the effective mass, and k is the momentum. In graphene the dispersion is linear close to the Dirac points:

$$E = \hbar v_F \sqrt{k_x^2 + k_y^2}, \quad (2.2)$$

where $v_F = 10^6$ m/s is the Fermi velocity of graphene. Hence, equation (2.1) is not valid in this case. Being linear for low energies, it mimics relativistic Dirac particles with zero effective mass. These properties are not only very exotic and give opportunity for fundamental studies of Dirac physics [45], but also mean that there is practically always an allowed optical excitation for any given wavelength, making the optical properties of graphene wavelength independent in a wide spectrum. The special way charge carriers behave in graphene, together with the possibility of

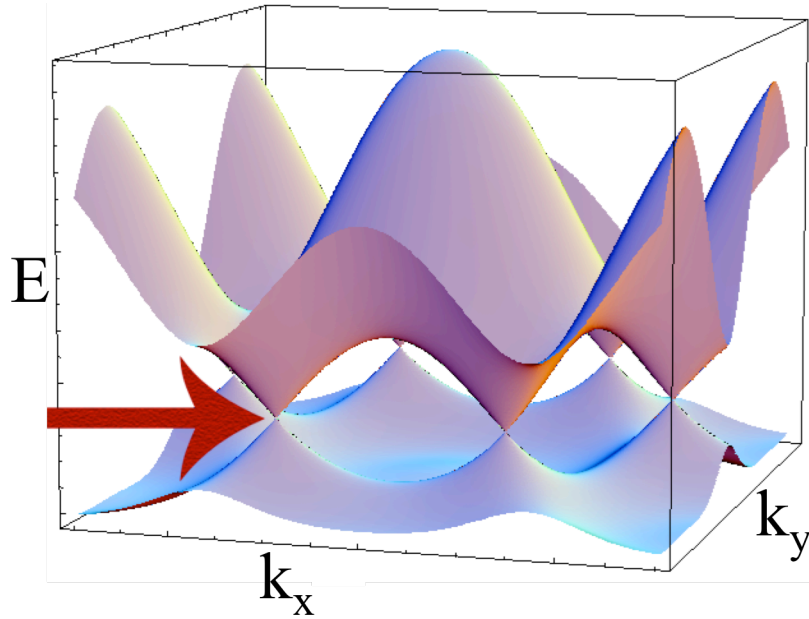


Figure 2.1: Dispersion relation for graphene. The conduction- and valence bands meet at six points in the Brillouin zone. Close to these points, the energy E is linear in momentum (k_x, k_y) . The arrow points at one of these Dirac points.

obtaining high quality graphene crystals, allow for both electrons and holes to exhibit very large charge carrier mobilities.

For a much more detailed review on the electronic properties of graphene, please see Castro Neto *et al.* [44].

2.2 Field effect

The heart of modern electronics is the field-effect transistor, where the electronic properties of a semiconductor are controlled by an external electric field. This effect is not seen in conventional metals due to the high charge carrier density and screening of the electrical field at very short distance. For the one atom thin semimetal graphene the capacitively induced surface charges in the order of 10^{13} cm^{-2} by a gate electrode are enough to drastically change the graphene properties [3]. Depending on the sign of the applied gate voltage, the carrier concentration can be tuned from holes to electrons, showing the bipolar field effect. Due to thermal fluctuations, non-uniformities in the graphene, impurities, electrical charges in the vicinity of graphene, etc., there is always a minimum residual charge carrier concentration n_0 in any graphene device despite tuning by gate. Further discussion on the doping mechanisms of graphene is given in Chapter 5.1.

Charge carriers in graphene can exhibit extremely large charge carrier mobility μ in the order of $10^5 \text{ cm}^2/\text{Vs}$ and $10^6 \text{ cm}^2/\text{Vs}$ at room temperature and at 4 K, respectively. Being essentially two surfaces and having no bulk, the environment easily affects the electronic properties of graphene. This renders both μ and n_0 highly dependent on the graphene fabrication and device processing.

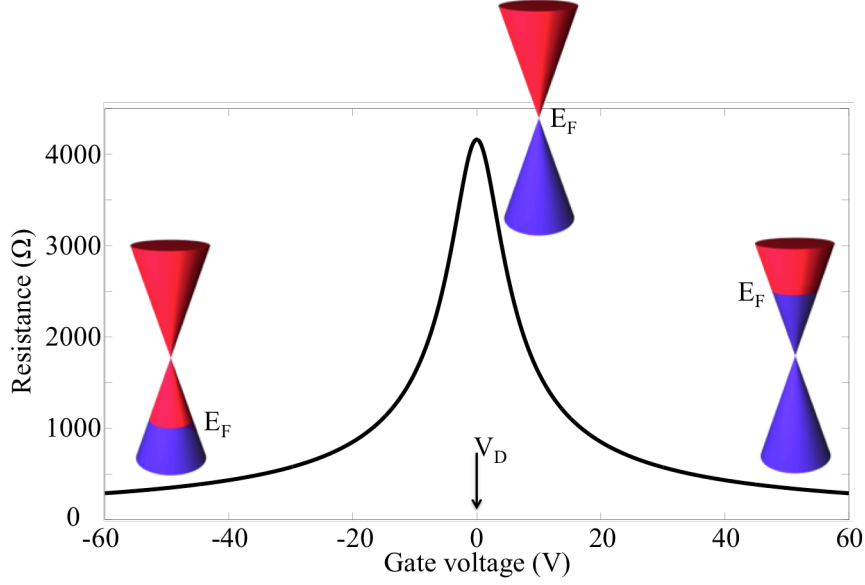


Figure 2.2: Calculated resistance as a function of gate voltage for graphene on 300 nm SiO₂ using equation (2.3). The parameters used in the calculation were: $R_{\text{contact}} = 0 \Omega$, $N_{\text{sq}} = 1$, $n_0 = 3.0 \cdot 10^{11} \text{ cm}^{-2}$, and $\mu = 5000 \text{ cm}^2/\text{Vs}$. V_D marks the Dirac point, where the resistance reaches its maximum. If the gate voltage is larger than V_D , the graphene is n doped (electron doped) and if it is smaller, the graphene is p doped (hole doped). E_F marks the Fermi energy.

Performing measurements where the carrier concentration is controlled by a gate in a transistor configuration is a powerful method to electrically characterize graphene. Assuming that both μ and the contact resistance R_{contact} are independent of charge carrier concentration, a diffusive model of the resistance R of the device can be used [46]:

$$R = R_{\text{contact}} + \frac{N_{\text{sq}}}{\sqrt{n_0^2 + n_g^2} e \mu}, \quad (2.3)$$

where N_{sq} is the geometrical number of squares of the device (length divided by width), n_g is the charge induced by the gate voltage Vg (parallel plate capacitor configuration, taking into account the quantum capacitance), and e is the elementary charge. As all resistance measurements in this work from which μ is estimated are made using a four-probe configuration, there should be no measured contact resistance. Hence, R_{contact} should be vanishing for the fit to be reliable. Resistance as a function of gate voltage (converted to gate-induced charge) is fitted to the above equation using R_{contact} , n_0 , and μ as fitting parameters. This is an efficient way to estimate the device mobility. Figure 2.2 shows resistance calculated as a function of gate voltage for a device with $R_{\text{contact}} = 0 \Omega$, $N_{\text{sq}} = 1$, $n_0 = 3.0 \cdot 10^{11} \text{ cm}^{-2}$, and $\mu = 5000 \text{ cm}^2/\text{Vs}$. The Dirac point, where the resistance reaches a maximum, is close to zero gate voltage where the minimum carrier density is present. In practical devices, the Dirac point is often shifted from zero voltage due to charged impurities in the vicinity of graphene.

It is also possible to obtain a rough estimate of the mobility directly from the Drude model of conductivity:

$$\sigma = ne\mu \Rightarrow \mu = \frac{\sigma}{ne}, \quad (2.4)$$

where $\sigma = 1/R_s$ is the conductivity and $R_s = R/N_{sq}$ is the sheet resistance. This can be differentiated to give an estimate of the mobility $\tilde{\mu}$, assuming a parallel plate capacitor configuration, to:

$$\tilde{\mu} \approx \frac{1}{e} \frac{\partial \sigma}{\partial n} = \frac{1}{e} \frac{\partial \sigma}{\partial V_g} \frac{\partial V_g}{\partial n} = \frac{1}{e} \frac{\partial \sigma}{\partial V_g} \frac{1}{C_g} = \frac{1}{e} \frac{\partial \sigma}{\partial V_g} \frac{d}{\epsilon_r A}, \quad (2.5)$$

where C_g is the specific capacitance, d is the distance between gate electrode and graphene, ϵ_r is the relative permittivity, and A is the overlapping area of gate electrode and graphene. This model is useful when the electronic quality of graphene is poor. In this case, resistance is not a symmetric function of gate voltage and equation (2.3) does not provide a good description.

2.3 Hall effect

When a magnetic field is applied perpendicularly to a current flowing in the conductor, charge carrier trajectories “bend” due the laterally oriented Lorentz force. This leads to a change in the resistance along the net current path (magnetoresistance) and a voltage buildup in the transverse direction (Hall voltage). Hall measurements provide a direct way to measure the charge carrier concentration in any conductor. Knowing the carrier concentration, the mobility can be calculated from the conductivity at zero magnetic field. Well-defined sample geometry is needed for accurate measurements.

Figure 2.3 shows the Hall effect measurement setup. A current I is applied through a graphene strip while voltages along (V_{xx}) and transverse (V_{xy}) the current path are measured. The longitudinal resistivity is given by:

$$\rho_{xx} = \frac{R_{xx}}{N_{sq}} = \frac{1}{N_{sq}} \frac{V_{xx}}{I}, \quad (2.6)$$

where R_{xx} is the longitudinal resistance. The Hall resistivity is given by:

$$\rho_{xy} = R_{xy} = \frac{V_{xy}}{I}, \quad (2.7)$$

where R_{xy} is the transversal resistance. From the Lorentz force we obtain the theoretical expression for the Hall voltage:

$$V_{xy} = \frac{IB}{nq}, \quad (2.8)$$

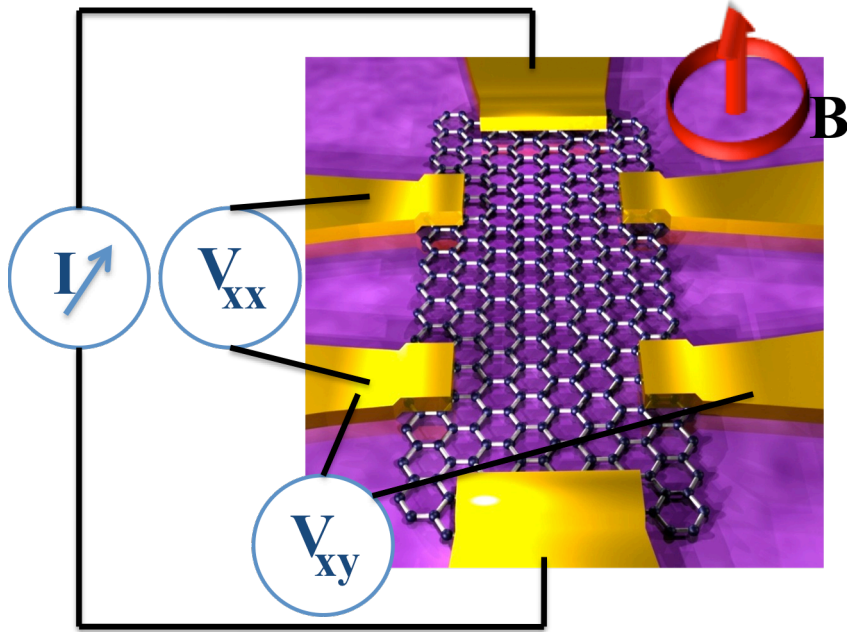


Figure 2.3: An illustration of a graphene Hall bar structure. A current I is applied and the longitudinal- and transverse voltages V_{xx} and V_{xy} are measured. The magnetic field B is applied perpendicularly to the current path.

where B is the applied magnetic field and q is the individual carrier charge, which can be either $-e$ or $+e$ for electrons and holes, respectively. We combine these expressions to obtain:

$$\rho_{xy} = \frac{1}{nq} B = R_H B, \quad (2.9)$$

where R_H is the Hall coefficient. R_H is obtained by a linear fit at moderate magnetic fields, typically less than one tesla. Via the Drude model in equation (2.4) we obtain an expression for the mobility, using the conductance at zero magnetic field:

$$\mu = \frac{\sigma}{e|n|} = \frac{\sigma}{e} \frac{V_{xy} e}{IB} = R_H \sigma \quad (2.10)$$

Hence it is possible to obtain the mobility independently from both field- and Hall-effect measurements.

2.4 Quantum Hall effect

Many interesting phenomena in two-dimensional systems occur at high magnetic fields [47] when the continuous density of states (DOS) is split into discrete levels with spacing larger than the thermal energy at low temperature. When the magnetic field is increased, so is the degeneracy of each level, forcing the Fermi level to decrease. In the case of graphene, it is also possible to fix the magnetic field and instead vary the Fermi energy using a gate electrode. Ideally, this splitting of energy

levels results in δ -peaks in the DOS, but due to thermal broadening, the peaks have a finite width.

Many of the system properties oscillate, including resistivity, as the Fermi level goes through the subsequent peaks in the DOS. As an example, resistivity oscillations are called Shubnikov-de Haas oscillations. Because the Fermi level lies between two peaks, there are no current-carrying states available, provided that the thermal broadening of the quantized levels is small enough. Hence the longitudinal conductance will vanish and so will the longitudinal resistivity, ρ_{xx} . While there are no current-carrying states in the bulk, there are edge states, which do carry current. The Hall resistance ρ_{xy} becomes quantized at this point. This is the IQHE [48].

In graphene, ρ_{xy} plateaus are given by [5, 49]:

$$\rho_{xy} = \frac{1}{g_s (l+1/2)} \frac{h}{e^2}, \quad l = 0, 1, 2, \dots, \quad (2.11)$$

where $g_s = 4$ is the degeneracy factor, including spin and sublattice degeneracies. This gives the following sequence:

$$\rho_{xy} = 12.9, 4.30, 2.58 \text{ k}\Omega, \dots, \quad (2.12)$$

which is different from the ordinary IQHE and is named half-integer quantum Hall effect. The different sequence comes from the unique band structure of graphene. Since no other known material possesses the same Hall plateau series, this can be taken as a signature of monolayer graphene. Bilayer graphene also exhibits an unusual, but different from that of monolayer graphene, series of plateaus.

2.5 Aharonov-Bohm effect

Charge carriers travelling through different trajectories in a conductor interfere due to their quantum mechanical nature. Applying different magnetic- or electrical fields modifies this interference, giving a characteristic $R(B)$ dependence. This dependence is irregular but reproducible, reflecting a characteristic distribution of scattering centers in a sample. Such irregular $R(B)$ is called universal conductance fluctuations (UCFs). It is not noise but a reproducible effect. UCFs are typically seen only at low temperature. Because of the large amount of different electron paths, the interference is complex and no periodicity is seen.

The electron paths are better defined if the graphene is shaped into a loop. Periodic interference from electron paths that encircle the loop occurs similar to the optical double-slit experiment. By applying a uniform, perpendicular magnetic field, \mathbf{B} with magnetic vector potential \mathbf{A} , a phase shift $\delta\phi$ between electron paths travelling on different sides of the loop is induced [50]:

$$\delta\phi = \frac{e}{\hbar} \int_{loop} \mathbf{A} \cdot d\mathbf{l} = \frac{e}{\hbar} \int_{area} \nabla \times \mathbf{A} \, d\mathbf{a} = \frac{e}{\hbar} \int_{area} \mathbf{B} \cdot d\mathbf{a} = \frac{e}{\hbar} aB, \quad (2.13)$$

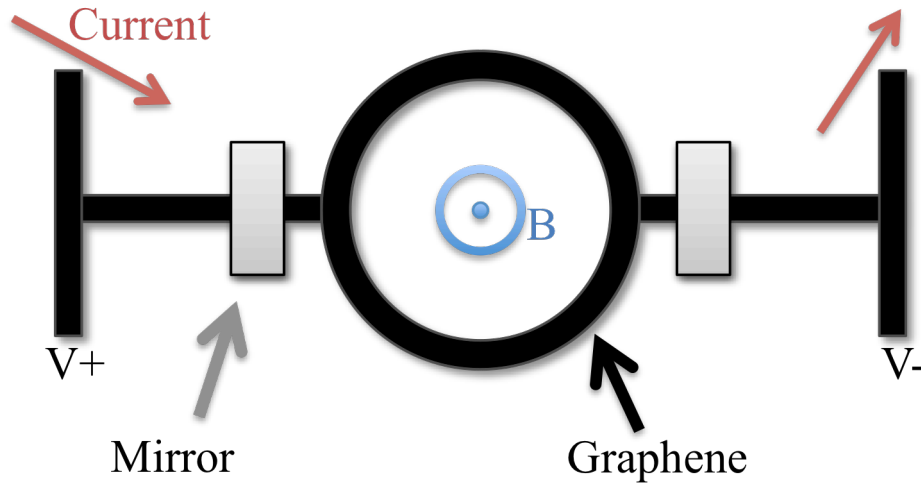


Figure 2.4: An illustration of an Aharonov-Bohm device. A current is applied through a ring structure in with a perpendicular magnetic field B while monitoring the resistance. Metal mirrors are deposited on the ring perimeter to confine charge carriers to the ring.

where a is the area of the loop and B is the magnitude of the magnetic field. Thus, the fundamental oscillation frequency is $e/h \cdot a$, where h is the Planck constant. If the coherence of the system is large enough, higher order oscillations, $N \cdot e/h \cdot a$, where N is an integer, also become visible. These correspond to charge carriers coherently encircling the ring more than once.

To improve the quantum coherence of the system, “mirrors” are put in the vicinity of the graphene ring [51-53]. Figure 2.4 shows the experiment layout. The mirrors serve the purpose of confining charge carriers to the ring by increasing scattering at its entry points. This can be understood as a Fermi velocity mismatch between the graphene and the deposited metal. In principle any material that increase the scattering of charge carriers traveling through the ring could improve the visibility of higher order Aharonov-Bohm oscillations.

At low temperatures, strong UCFs mask the Aharonov-Bohm oscillations. To distinguish between aperiodic fluctuations and the periodic oscillations originating from the Aharonov-Bohm effect, fast Fourier transform (FFT) analysis is utilized.

2.6 Optical visibility

Graphene absorbs only 2.3 % of visible light [15], making it very difficult to see when deposited on most substrates. It was essential for the isolation of graphene that the researchers happened to use silicon wafers with a thin layer of silicon dioxide, which had just about the right thickness for graphene to be visible. While it first happened by a fortunate coincidence, it is possible to engineer the sample layout to maximize the graphene visibility. Identifying graphene and determining the number of layers from the contrast in optical microscopy is a quick and powerful method.

We can calculate the contrast of graphene deposited on opaque substrates with a thin transparent film on top (typically an oxide) using a simple optical model [54].

Interference between incident and reflected light beams in the substrate-oxide-graphene structure gives rise to a contrast between graphene and the bare substrate, depending on wavelength and the oxide thickness. The same effect gives oxides like SiO₂ their familiar color on top of silicon.

An opaque substrate with refractive index \tilde{n}_3 is covered with an oxide layer with refractive index \tilde{n}_2 and thickness d_2 . Graphene is assumed to have the same refractive index as graphite $\tilde{n}_1 = 2.6 - 1.3 \cdot i$ and a thickness of 0.34 nm (the distance between graphene layers in graphite). The refractive index of air is $\tilde{n}_0 = 1.0$. The relative indices of refraction are denoted as:

$$r_1 = \frac{\tilde{n}_0 - \tilde{n}_1}{\tilde{n}_0 + \tilde{n}_1}, r_2 = \frac{\tilde{n}_1 - \tilde{n}_2}{\tilde{n}_1 + \tilde{n}_2}, r_3 = \frac{\tilde{n}_2 - \tilde{n}_3}{\tilde{n}_2 + \tilde{n}_3} \quad (2.14)$$

and the phase shifts due to the optical path as:

$$\Phi_1 = 2\pi\tilde{n}_1 d_1 / \lambda, \Phi_2 = 2\pi\tilde{n}_2 d_2 / \lambda \quad (2.15)$$

The reflected light intensity \tilde{I}_{op} can be calculated as:

$$\tilde{I}_{\text{op}}(\tilde{n}_1) = \left| \frac{\left(r_1 e^{i(\Phi_1 + \Phi_2)} + r_2 e^{-i(\Phi_1 - \Phi_2)} + r_3 e^{-i(\Phi_1 + \Phi_2)} + r_1 r_2 r_3 e^{i(\Phi_1 - \Phi_2)} \right)}{\left(e^{i(\Phi_1 + \Phi_2)} + r_1 r_2 e^{-i(\Phi_1 - \Phi_2)} + r_1 r_3 e^{-i(\Phi_1 + \Phi_2)} + r_2 r_3 e^{i(\Phi_1 - \Phi_2)} \right)} \right|^2 \quad (2.16)$$

The contrast is defined as the relative difference in reflected light of areas with- and without graphene, respectively. The intensity from areas without graphene are calculated using the refractive index of air $\tilde{n}_1 = 1.0$:

$$\text{contrast} = \frac{\tilde{I}_{\text{op}}(\tilde{n}_1 = 1.0) - \tilde{I}_{\text{op}}(\tilde{n}_1 = 2.6 - 1.3 \cdot i)}{\tilde{I}_{\text{op}}(\tilde{n}_1 = 1.0)} \quad (2.17)$$

By varying both the wavelength of light and the thickness of the oxide, the contrast of graphene can be optimized. The result for graphene on top of SiO₂ is shown in Figure 2.5. The best contrast is achieved for either ~90 nm or ~290 nm of SiO₂ thickness. Using green light of ~550 nm wavelength, a contrast around 10 % can be achieved. This is more than twice than what is expected from the pure absorption of graphene.

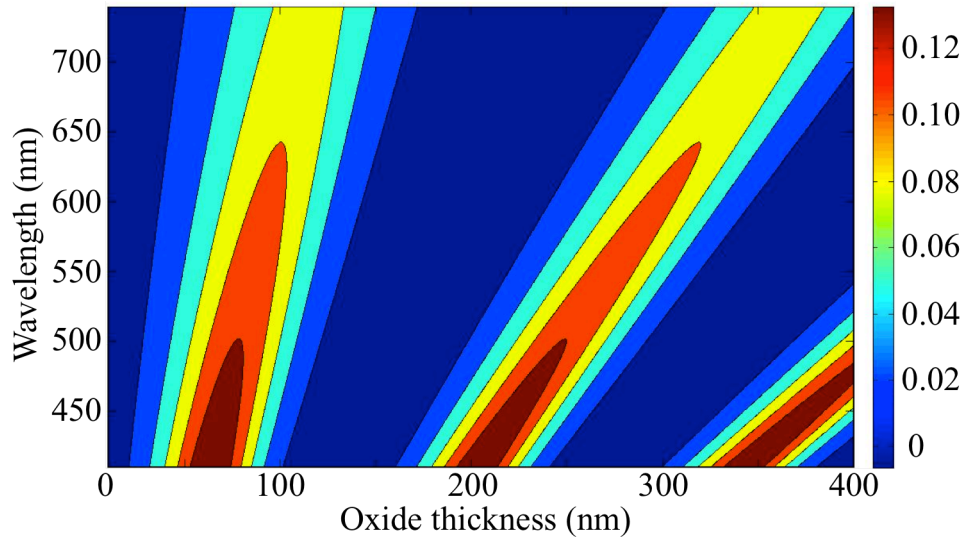


Figure 2.5: Color plot of the optical contrast of graphene on SiO_2/Si substrates as a function of wavelength and oxide thickness. The color scale shows the theoretical contrast.

SiO_2 on Si substrates is the most common setup used for graphene experiments. We also calculate optical contrast of graphene on a ferroelectric barium strontium titanate (BSTO) thin film on top of a Nb-doped strontium titanate (Nb-STO) substrate as a function of its thickness and the optical wavelength. Refractive indices of BSTO and Nb-STO were obtained using spectroscopic ellipsometry. The theoretical contrast as a function of BSTO thickness and incident wavelength is seen in Figure 2.6. The maximum contrast of graphene on BSTO / Nb-STO is lower than that on SiO_2/Si (3 % vs. 10 %), making graphene much more difficult to find on the former substrate. In this case we use atomic force microscopy (AFM) to distinguish atomically thin areas after identifying promising sites using optical microscopy.

While optical microscopy provides a fast technique to identify graphene, it has to be calibrated against other methods, which provide a direct signature of having a certain number of layers. In this work this is done using quantum Hall effect measurements as described in Chapter 2.4, allowing to distinguish between one-, two-, and multilayer graphene.

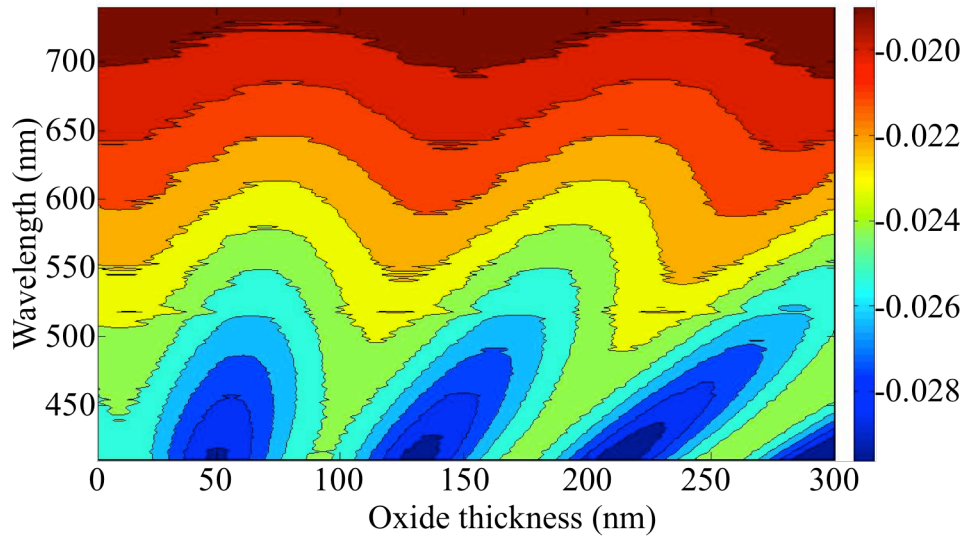


Figure 2.6: Color plot of the optical contrast of graphene on BSTO / Nb-STO substrates as a function of wavelength and oxide thickness. The color scale shows the theoretical contrast. The absolute value of the contrast is less than 3 % for any combination of wavelength and oxide thickness in the visible spectrum of light. Hence, there is no contrast enhancement from optical interference making it difficult to find graphene on such substrates.

3 Graphene fabrication

There exist many techniques for fabricating graphene, all with their own strengths and limitations. Since different techniques give materials with widespread properties, it is common to view graphene as a family of materials, rather than a single one.

The most common fabrication method is mechanical exfoliation, which is described in Chapter 3.1. While it is versatile and gives the highest quality graphene to date, the technique is not scalable and can only be used for research and development. The most promising scalable method is producing graphene by chemical vapor deposition (CVD) on metal catalysts. CVD of graphene on copper, the most common catalyst, is described in Chapter 3.2. While it is possible to obtain large-area high quality graphene with this technique, the transfer of graphene from metal catalyst to the target substrate introduces problems. For this reason we develop a catalyst- and transfer-free graphene CVD technique, which is described in Chapter 3.3.

Other techniques include the sublimation of Si from SiC [55], liquid phase exfoliation of graphite [56], reducing graphene oxide [57], and the chemical bottom-up approach [58]. These are, however, beyond the scope of this thesis.

In Chapter 3.4, nanofabrication procedures and the typical sample layout are presented.

3.1 Mechanical exfoliation

Graphene was initially produced by exfoliating graphite with sticky tape and depositing it on a substrate [4]. Many different graphite sources can be used. In this work, large crystals of high-purity natural graphite were chosen since they give large flakes with little contamination. The graphite crystal is cleaved several times using the tape. Large, uniform areas of thin graphite flakes on the tape are chosen by optical inspection and are then pressed against the desired substrate. Finally, the tape is carefully removed.

The mechanical exfoliation procedure results in a myriad of graphite flakes with varying thickness and lateral dimensions, with only a small minority being monolayer. Still, in most cases, at least one or a few graphene flakes are found. Figure 3.1 shows an optical image of a 50 μm long monolayer graphene flake on top of a

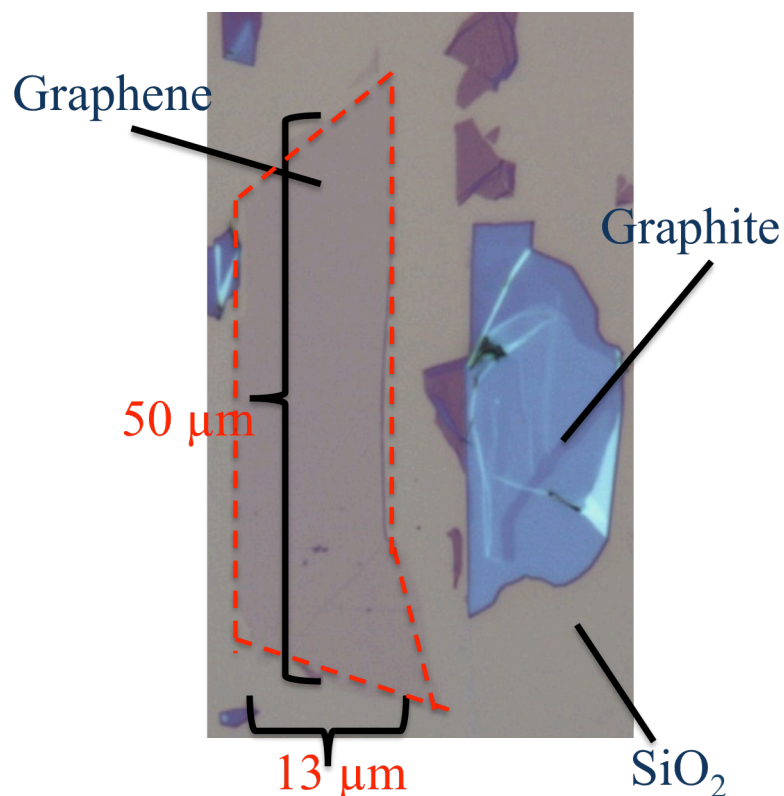


Figure 3.1: An optical image of a monolayer graphene flake on SiO₂ (outlined in dotted red). Thicker pieces of graphite are seen around it. Despite being atomically thin it is clearly visible under the microscope.

SiO₂ / Si substrate. Thicker pieces of graphite in the order of tens of layers are also seen.

While the size of flakes and the production throughput are limited, mechanical exfoliation remains the dominant technique for scientific purposes and for making proof of principle devices. Also, it produces the highest quality graphene.

3.2 Chemical vapor deposition on copper

Catalytic CVD of hydrocarbons on metallic substrates is the leading technology for scalable production of high-quality graphene. The size of graphene is essentially limited by the size of the growth furnace with 30-inch fabrication capabilities already realized [19].

In CVD, a substrate is exposed to one or several precursor gases containing reactive elements. These elements are made to react by heating the chamber to high temperature. In graphene CVD, typically three gases are introduced into the chamber. The primary atmosphere consists of Ar with a small amount of H₂. During the deposition phase, a carbon-containing gas is introduced to provide the material needed to grow the film. The Ar serves as a carrier gas to control the partial pressures of hydrogen and the carbon-containing gas. While the exact role of hydrogen in graphene CVD is not perfectly understood, it was suggested in reference [59] that H₂

serves several purposes. First, it helps the formation of sp^2 bonds. Second, it etches the weaker carbon-carbon bonds, assisting the formation of high quality bonds. Third, it reduces any oxide that may remain on the metal catalyst.

The carbon-containing gas is almost completely decomposed at the high temperature used in graphene CVD (>1000 °C). Free carbon atoms attach to- and diffuse at the surface and form chemical bonds to each other. The sp^2 bonds are the most stable and thermodynamically favorable for carbon but the temperature, while high, is still too low for the efficient creation of a large-scale sp^2 -hybridized carbon lattice. However, with the use of a metal catalyst as substrate, the energy barrier for creating such bonds is lowered and the film grows efficiently. The metal catalyst is essential for forming high quality bonds between the carbon atoms. As in many thin film deposition techniques, a high temperature and a low deposition rate favor high quality crystal growth. Therefore, the deposition temperature is kept close to melting point of the metal catalyst and the partial pressure of the carbon-containing gas is kept as low as possible.

Graphene was early grown on nickel substrates [60, 61], partly inspired by the CVD fabrication procedure for CNTs [62]. At high temperature, hydrocarbons decompose and carbon dissolves in the Ni substrate. Carbon segregates at the surface upon cool down thereby forming graphene. This results in a film with a varying number of graphene layers. Also, it is very sensitive to catalyst preparation and process timing.

In contrast, due to the low carbon solubility, the growth process of graphene on copper is dominated by surface chemical reactions [19, 63, 64]. The copper surface catalyzes both the decomposition of carbon precursor and the graphene formation. After the growth of one graphene layer, the surface-catalyzed reactions are screened, suppressing further growth. This results in large-area coverage of predominately monolayer graphene, with a few percent coverage of bi- and multilayers [65, 66]. Since the process is largely self-limiting it is less sensitive to the process parameters. The highest quality CVD-grown graphene is produced on copper catalysts [67].

We grow high quality graphene on Cu foils. It is also possible to use evaporated Cu thin films as catalysts but they produce worse quality graphene and are beyond the scope of this thesis [68-70]. An overview of the CVD chamber and a temperature profile for a typical growth process is shown in Figure 3.2(a) and (b), respectively. High purity Cu foil (50 μm thick, 99.995 % or 99.9999 % purity) is cleaned using acetone and isopropanol to remove organic contaminants and treated using acetic acid to remove the native copper oxide, prior to growth. The Cu foil is loaded into a cold-wall low-pressure CVD system equipped with a graphite Joule heater. The temperature is measured by a thermo-couple in contact with the copper. Gases are premixed in a quartz shower head to produce a uniform vertical gas flow.

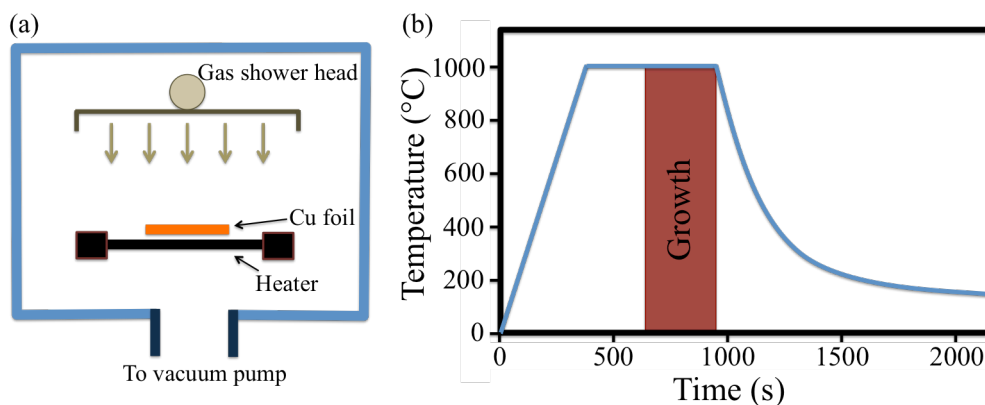


Figure 3.2: (a) A schematic overview of the CVD chamber. The gases are pre-mixed in the shower head and evenly introduced across the copper foil. The copper foil sits directly on a graphite Joule heater. The temperature is measured by a thermocouple connected directly to the copper. (b) Temperature profile of a typical graphene deposition on copper. Rapid ramping of temperature is used for both heating and cooling.

The system is first pumped to <0.1 mbar. Then heating is performed in a flow of 20 sccm H_2 and 1000 sccm Ar. The temperature is ramped to 1000 °C at a rate of 300 °C/min. The catalyst is annealed for 5 min to increase the domain sizes of Cu and to stabilize the system parameters. The growth is conducted using CH_4 (methane) as carbon precursor at a flow of 30 sccm for 5 min. CH_4 is preferred because it has high decomposition temperature and only one C atom per molecule [71]. The CH_4 is pre-diluted in Ar with only 5 % of CH_4 (99.9995 % pure). Hence, the partial pressure of carbon precursor is only $9 \cdot 10^{-3}$ mbar at a total pressure of 6.4 mbar. This is significantly lower than what was previously reported for graphene growth on Cu [72, 73]. The motivation is to achieve a lower deposition rate, a decreased density of nuclei, and to suppress the formation of multilayer graphene. It has been suggested that such conditions are too extreme [74]. However, assuming complete decomposition of CH_4 and 100 % sticking of carbon atoms to the Cu, there is enough carbon to grow more than 150 layers/s. While these assumptions are not always valid, we will show that the partial pressure of carbon is indeed high enough to grow a continuous graphene layer.

For the graphene to be characterized and used for electronic devices, it is necessary to transfer it to a dielectric substrate. Transferring large-area graphene while maintaining high uniformity and good electrical properties is a non-trivial task. Wet transfer methods are the most common while dry transfer in principle is possible [75]. A thin layer of MMA(8.5)MAA (EL10) copolymer is spin-coated on the top side of the Cu foil after growth and heated to 160 °C for 5 min. The copolymer acts as a mechanical support for graphene after the copper is removed. Graphene also grows on the bottom side of the foil since the gases can easily penetrate a gap between the foil and the heater, but the quality is not very reproducible. Oxygen plasma etching is used to remove graphene from the bottom side of the Cu foil.

Many different chemicals can be used to etch copper. The etching time strongly depends on the choice of etching agent and its concentration. Some strong acids like

HNO₃ quickly remove Cu, but can damage the copolymer and dope the graphene if not sufficiently diluted. FeCl₃ and other ionic salts can also be utilized avoiding acids completely, but they are inefficient in removing common copper contaminants, like iron, and result in residues after transfer. Another possibility is to use HCl, adding a very small amount of oxidizing hydrogen peroxide (H₂O₂). While HCl cannot etch copper, the small amount of H₂O₂ promotes slow oxidation of Cu. HCl then removes the copper oxide. For graphene described in this thesis, either diluted HNO₃ or diluted HCl with a small amount of added H₂O₂ are used.

When the etching is complete, the etchant is exchanged for water. The water is subsequently exchanged several times to remove as much of the etching residues as possible. At this point the graphene is attached to the rigid copolymer support and is in water. The desired target substrate is submerged into the water and the graphene / copolymer is placed on top. A piece of tape is attached to the top of the copolymer prior to etching to facilitate handling in liquid. Water is carefully removed from the beaker, leaving the graphene / copolymer lying on the target substrate. It is left drying in air for half an hour and then heated to 160 °C for 5 min to improve adhesion. Finally, the copolymer is removed in acetone and the graphene is successfully transferred to the target substrate. A photograph of transferred graphene is shown in Figure 3.3.

3.3 Chemical vapor deposition on insulators

Graphene CVD on copper foils is capable of producing large-area high quality graphene of good uniformity. However, the necessary transfer from metal catalyst to dielectric substrate, which is needed in almost any application, introduces several issues. These include wrinkle formation, holes and cracks in the graphene, added doping from chemicals and polymers used, and etching residues. While it is possible to optimize the transfer process and limit these effects, they cannot be completely avoided. Also, the wet transfer method is not easily integrated in semiconductor

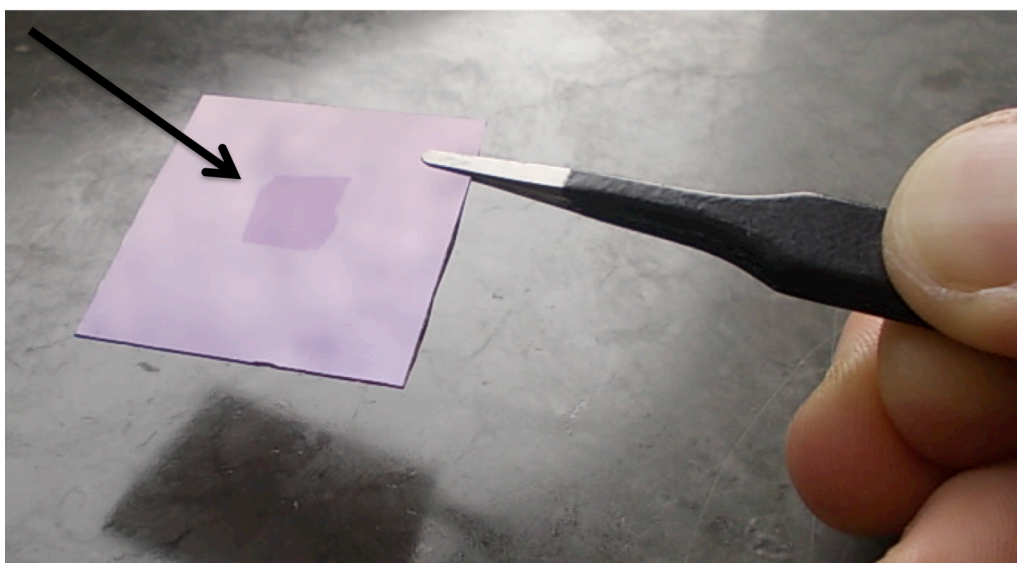


Figure 3.3: Photograph of Cu-grown graphene transferred to 300 nm SiO₂. The arrow points at the graphene, which is easily visible by the naked eye.

device fabrication. Hence, a transfer-free CVD method is desired.

We found that it is possible to grow nanocrystalline graphene directly on insulating substrates including SiO₂ [76, 77], HfO₂ [78], Al₂O₃ [77, 79, 80], Si₃N₄ [78], and practically any other high temperature compatible planar material by CVD [77]. Other groups also find similar results for ZnS [81], MgO [82], and BN [83]. Previously, attempts have been made to grow graphene directly on insulators but they yielded discontinuous graphene or graphene with unknown electrical properties [70, 83, 84].

We believe that contrary to the growth process of graphene on metals, this is a non-catalytic reaction where the hot and flat substrate merely serves as a template for graphene formation. The formation mechanism is further discussed in Chapter 4.3 in light of the experimental results. Synthetic graphite is normally produced at >3000 °C and catalysts are needed to lower the growth temperature as described earlier [85]. However, nanocrystalline graphite can be grown at much lower temperature. While graphene grown non-catalytically share some of the properties of large-crystal graphene, its electrical properties are worse. For many applications, however, it may still prove useful. Since the graphene grows directly on insulating substrates, there is no need for transfer and hence any transfer-related issues are avoided. Also, it makes the integration into semiconductor processing easier.

A typical process for the direct growth of graphene on SiO₂ / Si substrates is as follows. The growth chamber is the same as is described in Figure 3.2(a). Instead of the copper foil, SiO₂ / Si chips are put on the graphite heater. After evacuating the growth chamber, a flow of 20 sccm H₂ and 1000 sccm Ar is introduced. The system is heated to 1000 °C at a rate of 300 °C/min. An acetylene (C₂H₂) flow of 20 sccm is introduced during carbon deposition. The ambient pressure in the chamber is around 8 mbar with a 0.15 mbar partial pressure of acetylene.

Since this is not a surface catalytic process, it is not self-limiting but instead controlled by temperature, gas concentration, and the deposition time. The process is quite slow but reproducible. For the growth on SiO₂, a deposition time of 15-20 min yields a continuous film with optical properties similar to those of high quality monolayer graphene. If the growth is continued for a longer time, the optical transparency gradually decreases. Finally, the samples are cooled to room temperature in H₂ + Ar atmosphere.

The films are optically uniform independent of the growth time. Eventually tens of nanometer thick graphitic films are obtained having shiny color. Optical images of non-catalytically grown graphene on both opaque- and transparent substrates and using different deposition times are shown in Figure 3.4.

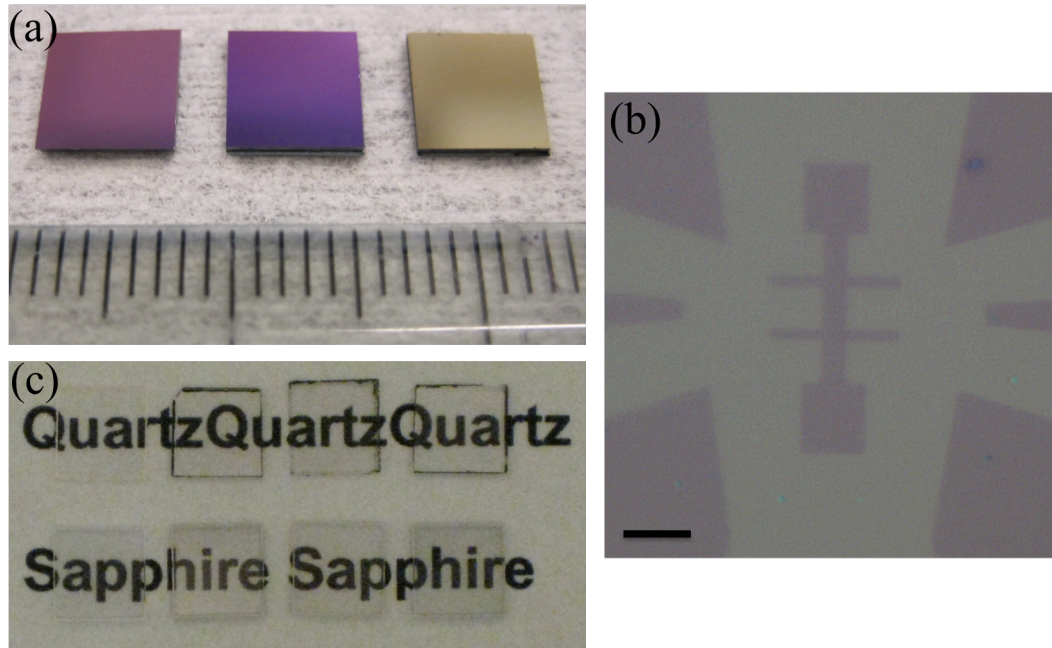


Figure 3.4: (a) Optical photograph of the 300 nm SiO_2 substrate (left), nominally monolayer graphene (middle), and ~ 70 nm thick shiny graphite (right). The substrates are $6 \times 6 \text{ mm}^2$. (b) Optical micrograph of non-catalytically grown graphene patterned into a Hall bar structure. The scale-bar is $5 \mu\text{m}$. (c) Optical photograph of graphene grown directly on transparent quartz (top row) and sapphire (bottom row). The substrates are $5 \times 5 \text{ mm}^2$.

3.4 Substrate layout and nanofabrication

This chapter describes the typical experimental platform for graphene experiments. Also, the most common nanofabrication techniques used to fabricate graphene devices are explained.

The most common substrate for graphene devices is highly doped silicon with a thin layer of silicon dioxide. In this thesis, Si substrates (n^{++}) with ~ 300 nm dry thermal SiO_2 are used if not stated otherwise. Such substrates give high graphene visibility as explained in Chapter 2.6. Due to the high doping of the Si substrate, it has metallic resistivity $< 0.005 \Omega\text{cm}$. Hence the substrate can be used as a back gate electrode with the SiO_2 layer acting as the gate dielectric. Figure 3.5 shows the typical sample layout. To be able to determine the position of a suitable graphene area and to find it in coming lithography steps, a grid of gold alignment marks is pre-patterned on the substrates. Graphene is put on top of the SiO_2 . It is then patterned and electrodes are deposited.

Two commonly used fabrication procedures will be presented in the following paragraphs. While a larger set of different techniques are used for the graphene processing, a majority of those are just varieties of the two described here.

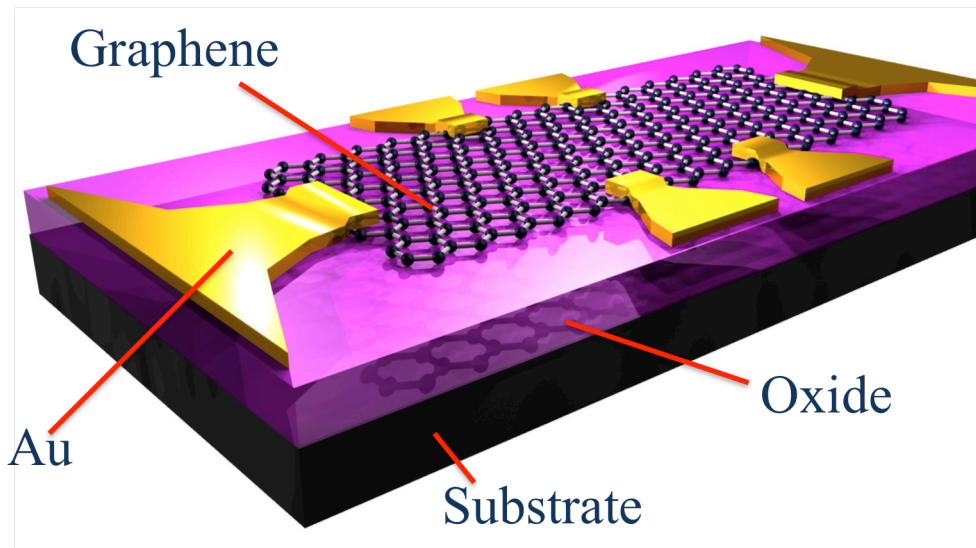


Figure 3.5: Typical sample layout. Graphene is deposited on an oxide lying on a opaque, conducting substrate. Au electrodes with either Ti or Cr adhesion layer are deposited on top.

Patterning graphene

Samples are first thoroughly cleaned in organic solvents. A thin (100 nm) layer of high-resolution positive electron beam lithography (EBL) resist (ZEP520A) is deposited using spin coating and cured on hot plate. The resist is patterned using EBL where a high-energy electron beam is scanned over parts of the sample. After exposure to the beam, the resist changes its chemical configuration making it solvable in certain liquids. O-xylene, an organic solvent, is used to remove exposed parts of the resist in our case. In this way, a desired pattern is transferred to resist. Unprotected by resist areas of graphene are then removed using a mild oxygen plasma etching. Finally, all the resist is removed using organic solvents. Figure 3.6(a-b) shows a graphene flake before- and after patterning, respectively.

Depositing electrodes

After cleaning with organic solvents, a double-layer resist stack consisting of copolymer underlayer (MMA(8.5)MAA (EL10), 350 nm) and polymethyl-methacrylate (PMMA, 60 nm) top layer are deposited by spin coating and cured on hot plate. The double-layer structure is utilized to create a certain profile in the resist where the top part is hanging out from the resist stack at the edges.

Resists are patterned by EBL and developed in a mixture of methyl isobutyl ketone and isopropanol. The top layer resist is sensitive to the electron beam as described above and selectively removed when developed. The bottom layer, however, does not require exposure but is solvable already. By controlling the development time, a certain amount of the bottom layer is removed, creating the desired profile of the resist stack.

Metal electrodes, typically gold with either a Cr or Ti thin underlayer to improve adhesion, are deposited by thermal- or electron beam evaporation. Finally,

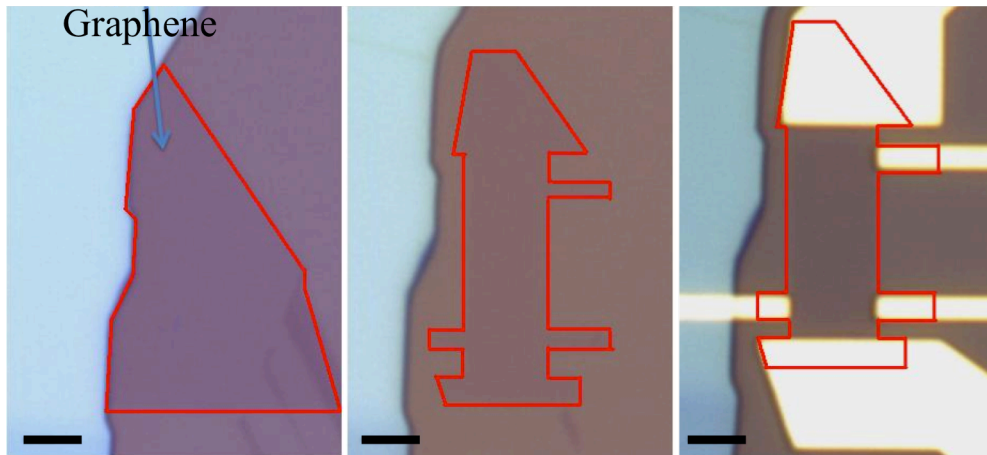


Figure 3.6: Typical graphene fabrication procedure. (a) A graphene flake, attached to a thicker piece of graphite, is located in optical microscope. The graphene is outlined in red. (b) The graphene is patterned by EBL and oxygen plasma etching. (c) Au / Ti electrodes are patterned and deposited in a second EBL step followed by electron-beam evaporation. All scale-bars are 2 μm .

the remaining resist stack is removed in a lift-off step. Figure 3.6(c) shows the final device with Au electrodes after lift-off.

More detailed recipes for two common lithography procedures are available in Appendix A.

4 Material characterization

Field-effect- and high magnetic field measurements are used to investigate the electronic properties of the different graphene materials described in Chapter 3. In Chapter 4.1, graphene produced by mechanical exfoliation is characterized showing excellent electronic properties and the IQHE. CVD-grown graphene on copper catalysts is shown in Chapter 4.2 and non-catalytically grown graphene in Chapter 4.3. For CVD-grown graphene, Raman characterization and electron microscopy images are also presented.

4.1 Graphene produced by mechanical exfoliation

Most of the interest in graphene is related to its electronic properties. By using the substrate as a back gate, a simple graphene field-effect transistor is realized. The electronic properties of the graphene device are extracted from measurements of graphene resistance while varying the voltage of the gate. Figure 4.1(a) shows a room-temperature four-probe measurement of resistance as a function of the gate voltage V_g minus the Dirac voltage, V_D . $V_D = -2$ V, indicating little n-type doping. An optical image of the measured device is shown in Figure 4.1(b).

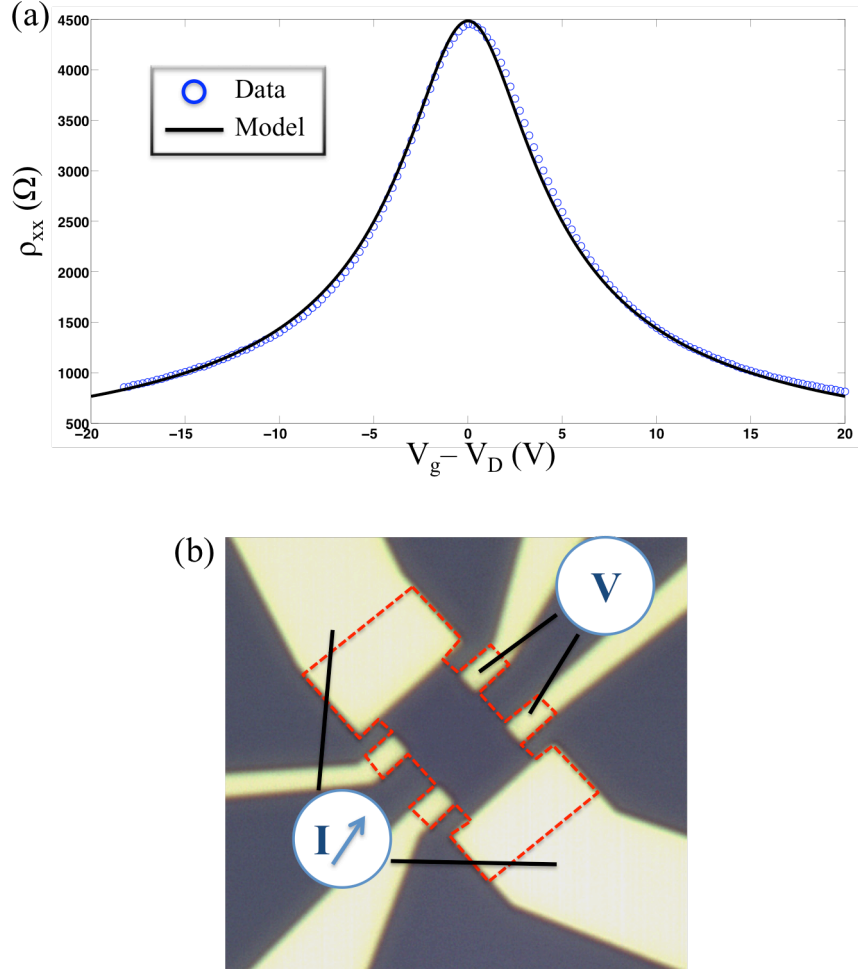


Figure 4.1: (a) Four-probe resistance as a function of $V_g - V_D$ at room temperature (blue circles) and the theoretical model (solid black line). From the model, we extract the values for $\mu = 5900 \text{ cm}^2/\text{Vs}$ and $n_0 = 2.4 \cdot 10^{11} \text{ cm}^{-2}$. (b) Optical micrograph of the device in (a). The graphene is outlined with the red dotted line.

The blue circles represent the measured data and the solid black line the numerical model described by equation (2.3). Extracted values for the mobility μ and the residual charge carrier concentration n_0 are $5900 \text{ cm}^2/\text{Vs}$ and $2.4 \cdot 10^{11} \text{ cm}^{-2}$, respectively. From the model we obtain negligible $R_{\text{contact}} = 40 \text{ } \Omega$, as expected from four-probe measurements. In a four-probe measurement, the contact resistance does not contribute. However, due to non-uniformities in the graphene, which are not taken into account by the model, a small value is obtained in the numerical model.

To further characterize the exfoliated graphene devices, they are cooled to cryogenic temperatures (4-20 K) and measured in high magnetic fields ($\lesssim 12 \text{ T}$). The mobility typically increases at low temperature. In Figure 4.2, ρ_{xx} and ρ_{xy} are measured as a function of magnetic field at 20 K. At high magnetic fields we first observe Shubnikov-de Haas oscillations and eventually the IQHE where the longitudinal resistivity ρ_{xx} vanishes. From the low-field behavior of the Hall resistivity ρ_{xy} we extract a carrier mobility of $\sim 7000 \text{ cm}^2/\text{Vs}$. At higher fields, ρ_{xy} accompanies the vanishing ρ_{xx} by saturating at a plateau of the theoretical value

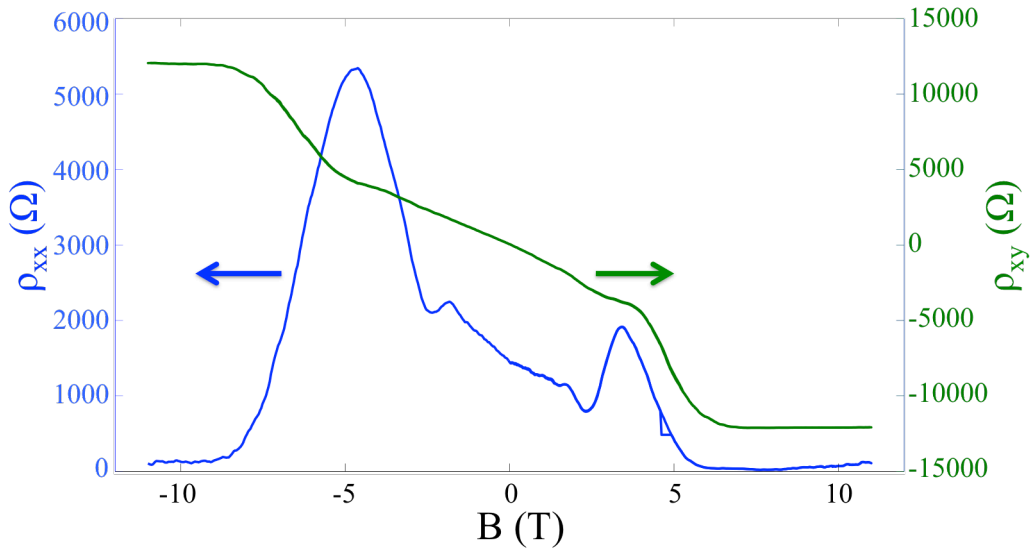


Figure 4.2: The integer quantum Hall effect in graphene at 20 K. At ~ 6 T, a Hall plateau becomes visible accompanied by vanishing longitudinal resistivity. This is the quantum Hall effect. For negative field similar behavior is seen. At lower magnetic fields, Shubnikov-de Haas oscillations are observed.

12.9 k Ω given by equation (2.11). The second plateau at 4.30 k Ω , is less visible. The observation of these features show that the sample is really monolayer graphene.

As described in Chapter 2.4, it is also possible to keep the magnetic field constant and instead vary the Fermi level by applying a gate voltage. This is shown in

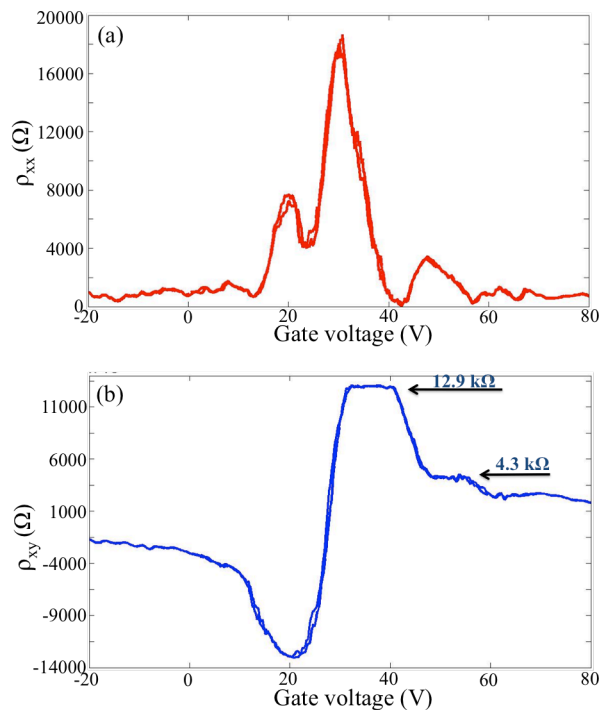


Figure 4.3: (a) Longitudinal resistivity as a function of gate voltage at 4 K and -11 T. (b) Corresponding Hall resistivity. Quantum Hall plateaus at 12.9 k Ω and 4.3 k Ω are clearly seen for positive gate voltages. The third plateau at 2.6 k Ω is less clear, but still visible. For negative gate voltages, no clear plateaus are seen.

Figure 4.3. The magnetic field is kept constant at -11 T while varying the gate voltage between -20 V and +80 V. Both the 12.9 k Ω and 4.30 k Ω plateaus are clearly seen in ρ_{xy} .

4.2 Graphene produced by catalytic CVD

The graphene grown on copper by CVD is transferred to standard SiO₂ / Si substrates for electrical characterization. Achieving a high uniformity and reproducibility is equally important as achieving a high mobility. Hence, many devices are fabricated on each chip to probe the reproducibility. Some devices are intentionally put at places that look optically uniform while others are placed at random. After optimizing the transfer process, high reproducibility is achieved for devices placed at favorable locations. However, sometimes when devices are located at random, the performance is poor, showing that there are areas in the material with inferior properties. This could be related to catalyst preparation procedures, temperature uniformity during growth, and the transfer process and will be studied further.

Room temperature field-effect measurements of three different devices on the same chip are shown in Figure 4.4(a). Four-probe resistance is shown as a function of

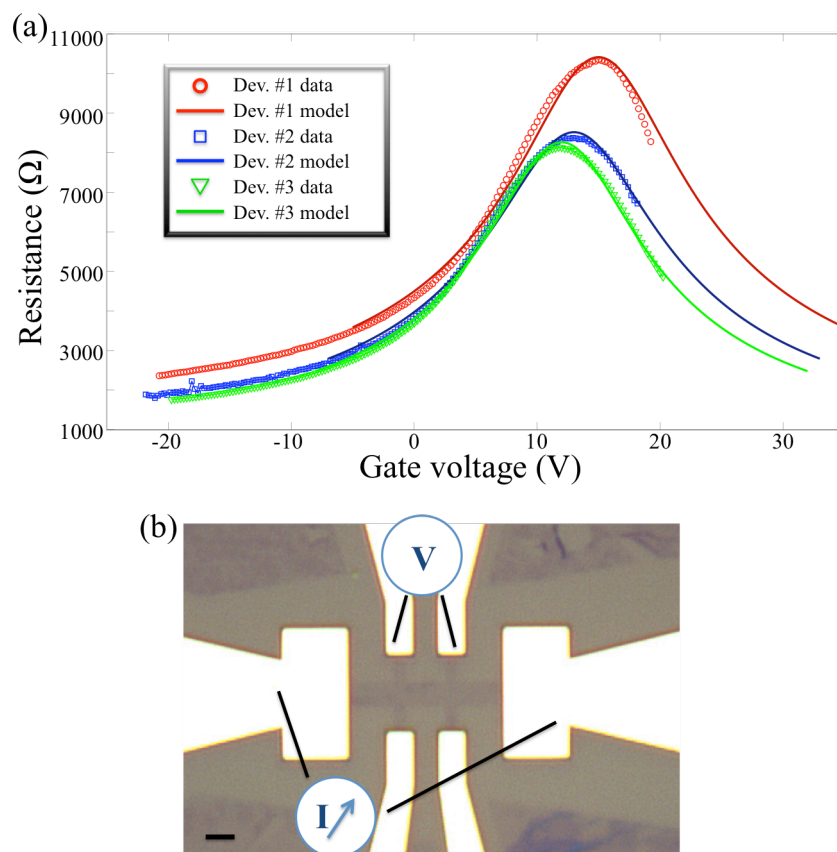


Figure 4.4: (a) Resistance as a function of gate voltage for three similar devices on the same chip. The graphene is grown on copper foil and transferred to SiO₂ / Si substrates. The devices exhibit similar doping with mobilities in the range 2600-3400 cm²/Vs at room temperature. (b) Optical image of one of the devices. The scale-bar is 2 μ m.

V_g together with the model fit of equation (2.3). The Dirac voltage was situated at ~ 15 V for all three devices having the same dimensions. Figure 4.4(b) shows an optical image of one of the devices. The mobility varies slightly between devices in the range 2600-3400 cm^2/Vs . The residual charge carrier concentration is in the range $4.4 - 4.9 \cdot 10^{11} \text{ cm}^{-2}$.

Measurements at low temperature and in high magnetic fields have not been performed for these samples. Previous samples, before improving the growth and transfer techniques, were measured at low temperature. They showed an increased mobility from 1200 cm^2/Vs to 1800 cm^2/Vs but no IQHE. Future work includes further experiments on CVD-grown graphene at low temperature.

Raman spectroscopy provides information about the quality of graphene, including the chemical configuration, the defect density, and the number of layers. It relies on the inelastic scattering of light from a monochromatic laser. The distribution of the inelastic scattered light is a direct probe of the low-frequency phonon modes of the system. A typical Raman spectrum for graphene grown on copper and transferred to SiO_2/Si substrates is shown in Figure 4.5 [86-88]. The strong 2D peak ($\sim 2683 \text{ cm}^{-1}$) with intensity larger than twice that of the G peak ($\sim 1591 \text{ cm}^{-1}$) can be fitted with a single Lorentzian. This shows that it is monolayer graphene of high quality. There is also a small D peak ($\sim 1350 \text{ cm}^{-1}$) indicating some disorder in the film.

Transmission electron microscopy (TEM) imaging of the Cu-grown graphene was also performed and is presented in the end of Chapter 4.3.

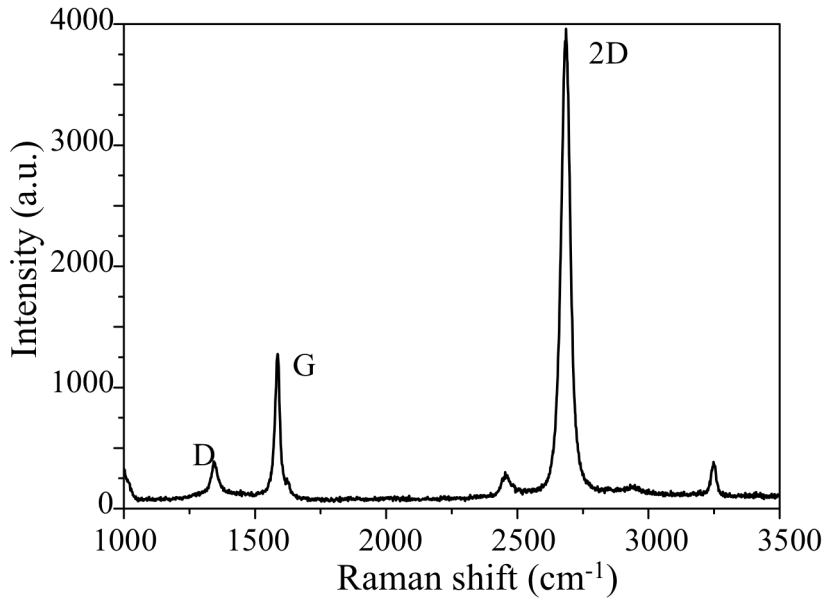


Figure 4.5: Raman spectrum of Cu-grown graphene transferred to SiO₂ / Si substrates. The 2D peak can be fitted with a single Lorentzian and its intensity is more than twice than that of the G peak, which is characteristic for monolayer graphene. There is also a small D peak indicating some disorder in the film. Peaks at 2450 cm⁻¹ and 3250 cm⁻¹ are attributed to higher-order Raman signals.

4.3 Graphene produced by non-catalytic CVD

Graphene grown non-catalytically directly on insulators show much smaller grain size and worse electronic properties compared to catalytically grown graphene. Field-effect measurements of graphene grown on Si₃N₄ are shown in Figure 4.6(a). The graphene used in this particular device shows optical properties similar to those of regular high-quality graphene. Upon applying gate voltage in the range $-20 V$ to $+40 V$, there is only about 25 % modulation of resistance. While this value is larger than in any metallic material prior to graphene, it shows that the mobility is very low. With such poor performance we cannot apply the model described by equation (2.3) but instead the mobility can be estimated directly from the less sophisticated model described by equation (2.5). It is in the order of tens of cm²/Vs, varying only slightly with the target substrate. We also measure samples in magnetic fields at both room- and low temperature. From these measurements, the extracted mobilities are in the same range as mentioned previously and do not vary significantly with temperature. A strong negative magnetoresistance is observed, even at room temperature, characteristic of disordered carbon materials [89-94]. We fit such data by the theory of weak localization to extract the dephasing lengths of the system. These increase from 6-7 nm at room temperature to 10-11 nm at 4 K (for data and a full description, see reference [76]), giving an indication of the typical scattering lengths in the system.

Raman measurements of graphene grown on SiO_2 are shown in Figure 4.6(b). We observe G and 2D peaks at $\sim 1591 \text{ cm}^{-1}$ and $\sim 2683 \text{ cm}^{-1}$, respectively, but the features are less sharp than in the case of catalytically grown graphene. These peaks are characteristic features of graphitic sp^2 -hybridized materials. The distinct peaks differentiate this material from amorphous carbon ($\alpha\text{-C}$), where very wide D and G bands merge together and there is no 2D peak [86, 95-97]. The D peak at 1350 cm^{-1} is very pronounced in non-catalytically grown graphene, indicating high disorder. We attribute this to the small grain domain size of this type of graphene compared to the laser spot in the Raman system which is $\sim 10 \mu\text{m}$. Hence the spot covers numerous domains leading to the large D peak. The length scale of disorder is roughly estimated by analyzing the intensity ratios of the D (I_D) and G (I_G) peaks, I_D/I_G , to be $\sim 7\text{-}8 \text{ nm}$ [98].

To directly observe the microscopic structure of the graphene, it is transferred to transmission electron microscopy (TEM) grids consisting of an irregular holey carbon network supported by a copper matrix structure using similar techniques as described in Chapter 3.2. These are loaded into a TEM operating at a low acceleration voltage ($\lesssim 80 \text{ kV}$) so as not to induce structural damage to the graphene while imaging [99-102]. Both graphene grown on copper and on insulators are analyzed in TEM. In Figure 4.7(a), a SEM image of Cu-grown graphene transferred to a TEM grid is shown. The graphene can span freely over holes with a diameter up to $\sim 10 \mu\text{m}$. Diffraction patterns in TEM are presented in Figure 4.7(b) [103] and (c-e) [104] for Cu-grown and non-catalytically grown graphene, respectively. Graphene grown on copper shows the characteristic hexagonal diffraction pattern of monolayer graphene, as expected. For non-catalytically grown graphene, it is also possible to see the diffraction pattern if the beam spot is focused to only $\sim 10 \text{ nm}$. For larger beam sizes,

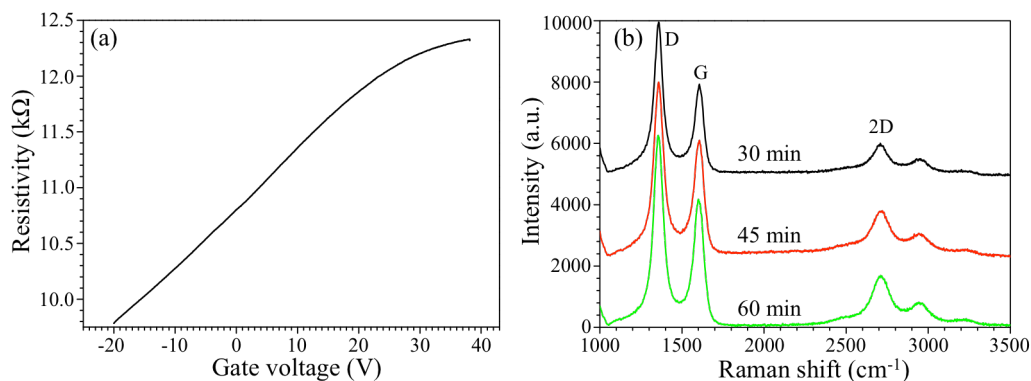


Figure 4.6: (a) Resistivity as a function of gate voltage for graphene grown directly on 100 nm thick Si_3N_4 . The resistivity is modulated $\sim 25\%$ for gate voltages between -20 V and $+40 \text{ V}$. The Dirac point is not visible, which is typical for this kind of graphene. (b) Raman spectrum for graphene grown on SiO_2 for 30 min (top), 45 min (middle), and 60 min (bottom). These films show distinct 2D and G peaks, which is characteristic for graphitic carbon. There is also a strong D peak, indicating significant disorder in the films. Curves are shifted along the ordinate for clarity.

hexagonal patterns from many different graphene domains are obtained. This indicates that the domain size of this material is in the order of ten nanometers, which is consistent with the results obtained from Raman characterization and magnetotransport measurements.

The non-catalytic graphene possesses quite different properties than those of large-crystal graphene obtained from mechanical exfoliation and catalytic CVD on copper. The fundamental difference is the crystal domain size. The reason for this is the different growth mechanisms. Non-catalytic graphene is named such since there is no evidence of catalytic activity of the substrate during film formation. On the contrary, the process is not self-limiting and only weakly dependent on the substrate material. Instead it is believed that graphene flakes form already in the gas phase. At 1000 °C, most of the methane or acetylene has already decomposed. The carbon atoms interact and form chains and small sp^2 -hybridized crystallites. Some of these will adhere to the hot and flat target substrate. Larger flakes have a higher probability of staying on the substrate. Light flakes will not sustain the high-energy thermal vibrations of the substrate but will detach. The temperature in our case is still too low to promote realignment and orientation of such larger flakes on the hot

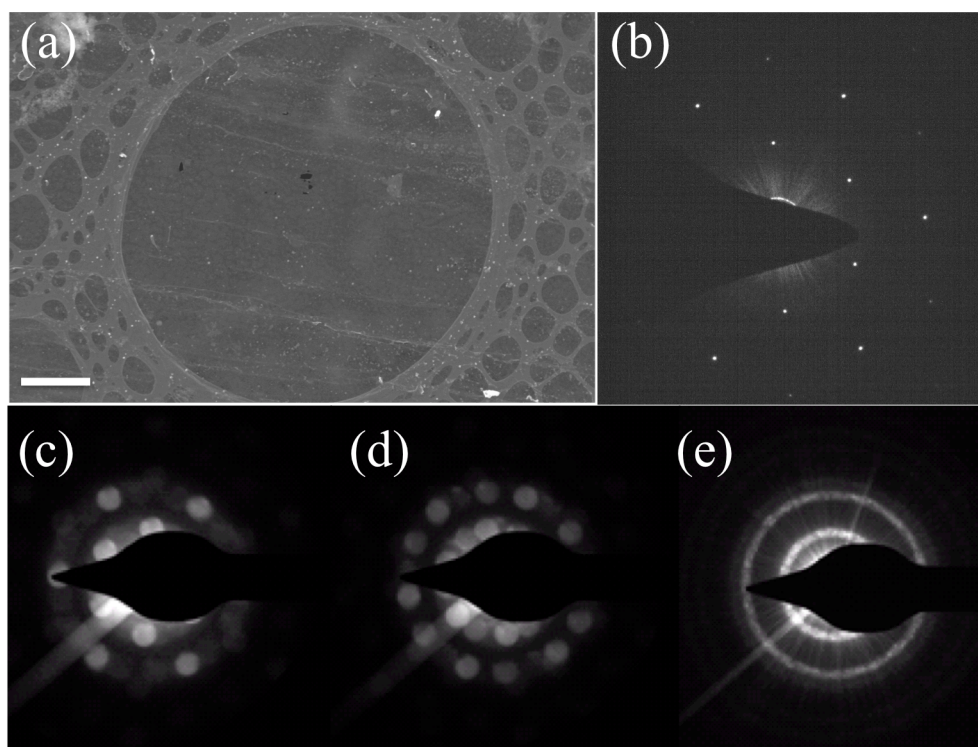


Figure 4.7: (a) SEM micrograph of Cu-grown graphene transferred to a holey carbon TEM grid. The graphene spans holes with diameter up to $\sim 10 \mu\text{m}$. The scale-bar is $2 \mu\text{m}$. (b) Diffraction pattern in TEM of similar graphene. It clearly shows the hexagonal signature pattern of monolayer graphene. Image obtained by Olof Bäcke. (c) TEM diffraction pattern for non-catalytically grown graphene for a focused beam of diameter $\sim 10 \text{nm}$. For larger beams, hexagonal patterns from two or more domains are observed as seen in (d) and (e), respectively. This shows that the domain size is in the order of $\sim 10 \text{nm}$. Images in (c-e) are obtained by Tim Booth.

substrate [105]. At yet lower temperature, carbon black will be formed [106-108]. Carbon black is essentially a 3D material consisting of chaotically oriented graphitic flakes. In our case such a process can be engineered to produce textured graphene films using a hot and flat substrate, high carbon gas concentration, and high temperature.

5 Cleaning using atomic force microscope

Pristine graphene possesses extraordinary electronic properties. However, the graphene is easily affected by surface contaminants. In this chapter, a straightforward mechanical technique to obtain atomically smooth graphene is presented. In Chapter 5.1, doping sources and cleaning techniques for graphene are discussed. Then in Chapter 5.2, the mechanical cleaning technique is described as well as the experimental results.

5.1 Introduction

Graphene is essentially two surfaces and no bulk making it easily affected by its environment. Charged impurities, surface contaminants, and structural deformation all contribute to local doping of graphene. This leads to an inhomogeneous charge density, the so-called electron-hole puddles and a shift in Dirac voltage V_D [109-113].

While clever choices of materials and chemicals are needed to limit contamination, residues from fabrication are inherent in any graphene processing. These act as external scattering centers and affect the device properties [114-120].

Several techniques exist for cleaning graphene. Standard cleaning using solvents is not sufficient to remove all these residues. The most commonly used cleaning technique is annealing at high temperature, typically ~ 400 °C in Ar / H₂ environment [67, 114, 116, 118, 121]. This technique is able to remove most of resist residues through desorption, but the coupling between the substrate and graphene may increase, leading to mechanical deformation of the graphene [120]. Also, temperature cycling of only 100–200 K causes rippling of suspended graphene [122]. Both these effects can cause degradation in device performance. Additionally, many substrates cannot sustain high temperature treatment. Some other can, but not without oxygen atmosphere, which is incompatible with graphene. One such example is ferroelectric BSTO thin films on Nb-STO substrates. Due to the polarized surface, charged contaminants adhere very strongly to these substrates. This renders graphene on BSTO heavily contaminated and difficult to clean.

Another similar method is annealing by Joule heating [115, 123]. This technically simple technique can be done in many setups, including in situ in a cryostat. Also with this method, graphene is heated locally to high temperature leading to rippling or even breakage if too much current is applied.

Just recently, mechanical cleaning of graphene was suggested as an alternative [124-127]. It is possible to use the mechanical cleaning method to obtain clean, atomically smooth graphene. The tip of an AFM is scanned in direct mechanical contact with graphene, removing contaminants in broom-like movements. Resist residues are efficiently brushed away, piling up outside the graphene flake. This technique produces atomically smooth graphene with improved electronic properties.

5.2 Experiment and results

AFM is used in tapping mode to observe the devices before and after cleaning. In this mode, the AFM does not influence the graphene. Cleaning is then done in contact mode using several different AFM probes and different forces. This technique can be used on both mechanically exfoliated graphene and CVD-grown graphene. In this work, however, results will only be presented on exfoliated graphene.

Typical height and phase images of graphene devices on SiO₂ after fabrication

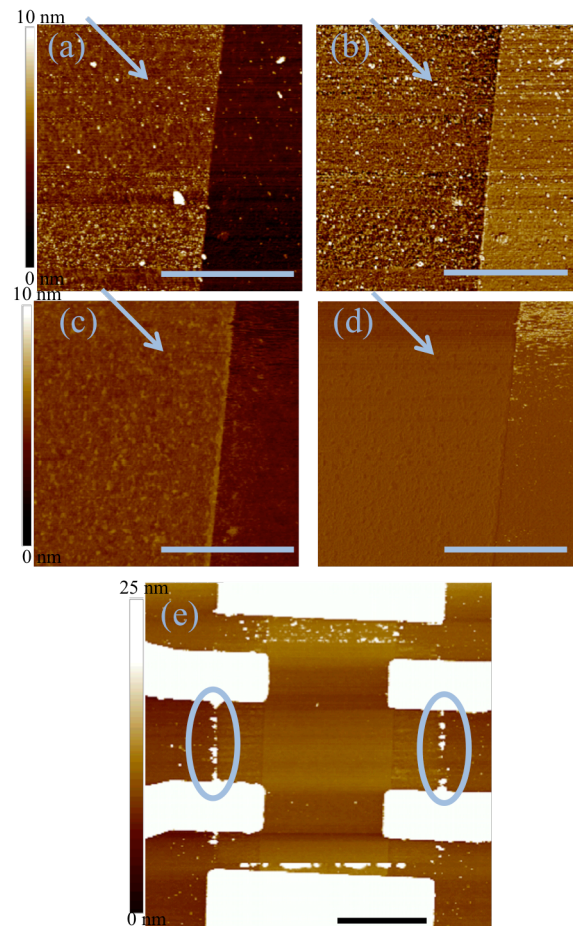


Figure 5.1: Tapping mode height (a) and phase (b) AFM images before cleaning. The device is contaminated and the graphene height RMS roughness is 0.77 nm. (c) and (d) Corresponding height and phase images after four scans in contact mode. The graphene height RMS roughness is reduced to 0.28 nm. The scale-bars in (a-d) are all 1 μm . (e) Overview AFM height image for a graphene device after cleaning. Only the central part was cleaned. The two ellipsoids mark beads with pushed-away contaminants. The scale-bar is 2 μm and the Z-scale is 25 nm.

are shown in Figure 5.1(a) and (b). The device is contaminated with resist residues with a height root mean square (RMS) roughness R_{RMS} of 0.77 nm and 0.47 nm for a $0.5 \times 0.5 \mu\text{m}^2$ area of graphene and bare SiO_2 substrate, respectively. The AFM is then set to contact mode, pushing the TiN-coated Si tip in direct contact with the sample. Contaminants are mechanically pushed to the sides in a broom-like way by scanning the tip back and forth over the sample. Typically three to five such scans are performed. The graphene is generally clean after only two scans and only minor improvement is seen with subsequent cleaning. In Figure 5.1(c) and (d) tapping mode images of the same area as in Figure 5.1(a) and (b) are shown after four scans in contact mode. R_{RMS} is now reduced to 0.28 nm and 0.29 nm for graphene and bare SiO_2 substrate, respectively.

To further clarify the effect of the cleaning, an overview AFM image obtained in tapping mode is shown in Figure 5.1(e). Only the central area of the device is cleaned in contact mode (both graphene and the surrounding substrate are cleaned). Around it, there are beads with pushed-away contaminants, as indicated by the two ellipses. The surface is significantly rougher outside the cleaned area.

R_{RMS} of SiO_2 is in the wide range 0.35–1.40 nm after fabrication. Corresponding values for graphene after fabrication are $R_{\text{RMS}} \sim 0.30\text{--}0.65$ nm. After cleaning, we obtain $R_{\text{RMS}} \sim 0.18\text{--}0.23$ nm and $R_{\text{RMS}} \sim 0.12\text{--}0.25$ nm for the bare substrate and graphene, respectively. Devices on both dry- and wet thermal oxide are studied. Wet oxide is rougher than dry oxide. However, the roughness of graphene depends more on the force applied in the AFM during cleaning than the type of oxide substrate. By using a stiff cantilever (NSG10 / TiN, spring constant $C \sim 15$ N/m) and a large contact force of 180 nN, the graphene is pushed down toward the substrate leading to similar roughness measurements of both bare SiO_2 and graphene ($R_{\text{RMS}} \sim 0.2$ nm). If instead, a softer cantilever (PPP-CONPt-20, $C \sim 0.17$ N/m) and smaller contact force of 30 nN are used, the graphene shows a significantly lower R_{RMS} than the bare substrate. For graphene a typical value of $R_{\text{RMS}} = 0.13$ nm is obtained.

The measured step height corresponding to graphene increases after microfabrication to around 1.5–2.0 nm. After cleaning it reduces to 0.6–0.7 nm, typical for clean graphene on SiO_2 [128].

To study the effect of the cleaning process on the electronic properties of graphene, samples are measured electrically before- and after cleaning. Field-effect measurements are performed at room temperature. We observe consistent changes in the Dirac point V_{D} after cleaning. After fabrication, devices are p-doped, showing a positive V_{D} in the range 12–24 V. After cleaning, V_{D} is found to shift to slightly negative voltages, indicating a weak electron doping probably induced by charges trapped in SiO_2 . In almost all cases, we also see an increased mobility after cleaning. However, the increase is only significant when using a small contact force while cleaning. In Figure 5.2(a), typical resistance measurements of a device cleaned using a small contact force are shown. V_{D} shifts from +12 V to -3 V while the mobility, estimated from the hole-branch of the curve, increases from ~ 4300 cm^2/Vs to ~ 7700 cm^2/Vs .

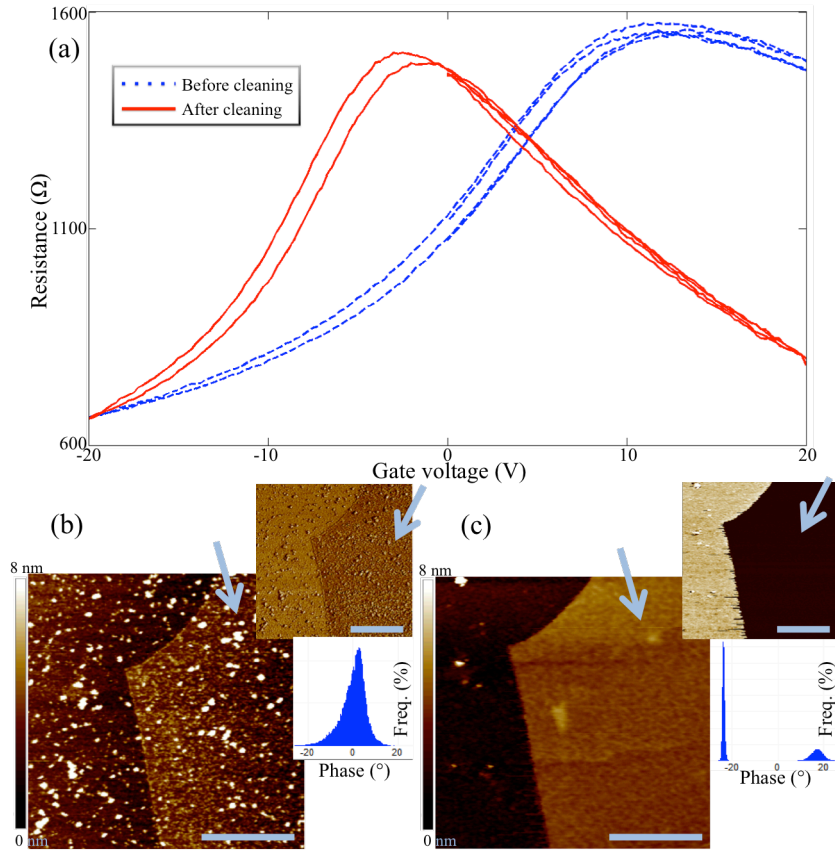


Figure 5.2: (a) Resistance as a function of gate voltage before (red, solid line) and after (blue, dashed line) cleaning. The Dirac point moves closer to zero after cleaning and the mobility increases from $\sim 4300 \text{ cm}^2/\text{Vs}$ to $\sim 7700 \text{ cm}^2/\text{Vs}$. (b) AFM height image of graphene on BSTO. Upper inset: AFM phase image. Lower inset: Histogram of surface roughness. Graphene on BSTO is heavily contaminated after fabrication with a graphene height RMS roughness of 1.82 nm. (c) Corresponding images after cleaning in contact mode. The graphene RMS roughness decreases to 0.17 nm and atomic steps become clearly visible in the BSTO film. The phase response changes from a broad distribution to two distinct peaks corresponding to graphene and the BSTO substrate, respectively. The arrows point at the graphene. The Z-scale is 8 nm.

To illustrate the effectiveness of the cleaning method, it is also employed to BSTO / Nb-STO substrates with graphene devices on top. Due to the polarization of the ferroelectric film, the contaminants are strongly adhered to the surface and are inherently difficult to remove. Height and phase (inset) measurements of graphene on BSTO after microfabrication are shown in Figure 5.2(b). With mechanical cleaning, it is possible to remove these well-adhered contaminants and recover atomically smooth graphene. In Figure 5.2(c), height and phase (inset) images of graphene on BSTO are shown after cleaning. The graphene becomes atomically flat after cleaning, with clearly visible atomic steps in the BSTO. R_{RMS} reduces from 1.82 nm (1.66 nm) to 0.170 nm (0.410 nm) for graphene (bare BSTO substrate). The phase response changes from a broad distribution to two distinct peaks at roughly -25° and $+20^\circ$, corresponding to graphene and BSTO, respectively.

5.3 Conclusions

Graphene is easily contaminated during nanofabrication processing, which affects its electronic properties. Mechanical cleaning of graphene using AFM is an easy way to obtain clean and atomically flat graphene. It improves the charge neutrality of graphene and, using moderate contact force, increases the mobility. Especially for samples that are incompatible with standard high temperature annealing cleaning processes, this technique appears to be indispensable, as in the case of graphene on BSTO.

6 Graphene on ferroelectrics

In combination with a ferroelectric substrate, graphene can be used as a read-out of the ferroelectric state. Thus realizing a memory device based on the ferroelectric state. Chapter 6.1 provides an introduction to the subject. In Chapter 6.2, the experimental results are shown and Chapter 6.3 provides conclusions.

6.1 Introduction

Graphene exhibits a strong field effect. The polarization of the ferroelectric results in a strong electric field. When graphene is put on top of the ferroelectric, its resistance is strongly dependent on the state of the ferroelectric.

Such devices were first produced by applying a ferroelectric polymer on top of standard graphene devices on SiO₂ [129, 130] and on flexible transparent substrates [131]. Few-layer graphene devices were realized directly on epitaxial ferroelectric oxide substrates [132]. In this work monolayer graphene devices on ferroelectric BSTO / Nb-STO substrates are studied. The Nb-doping renders STO opaque and, more importantly, metallic. Hence, it can be used as a back gate electrode, similar to the highly doped Si in ordinary graphene devices.

6.2 Experiment and results

The optical contrast of graphene on BSTO / Nb-STO is very poor due to the lack of interference-enhancement as described in Chapter 2.6. Still it is possible to find atomically thin flakes by very careful optical microscopy. Optical images before- and after deposition of Au / Cr electrodes of a graphene flake on BSTO are shown in Figure 6.1(a) and (b), respectively. It is not possible to determine the number of layers from optical images of graphene on BSTO. Thin flakes are identified optically and analyzed using AFM. Figure 6.1(c) and (d) shows AFM micrographs of the same flake as in Figure 6.1(a). The step height is ~0.5 nm indicating that it is monolayer, or possibly bilayer, graphene.

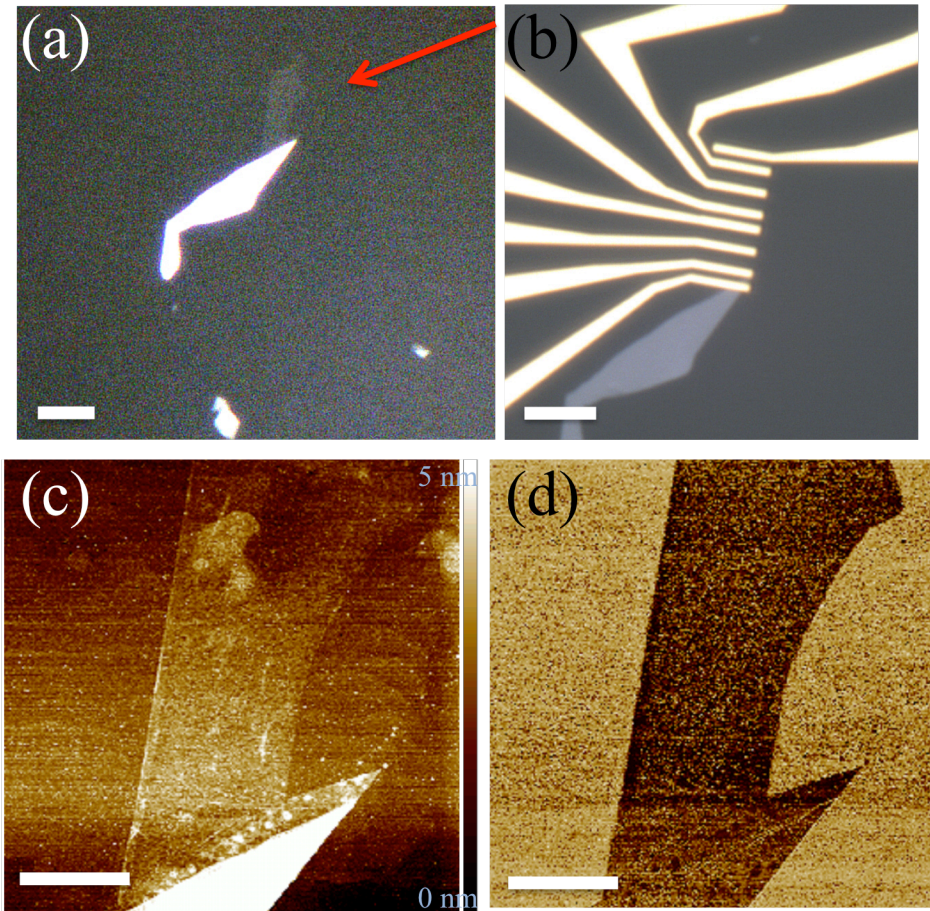


Figure 6.1: Optical micrographs of a graphene flake on BSTO before (a) and after (b) deposition of Au / Cr electrodes. The image in (a) is digitally filtered to make the graphene (pointed at by the red arrow) more visible. The graphene is attached to a thicker flake at its lower end. The scale-bars in (a) and (b) are both 5 μm . Tapping mode AFM height (c) and phase (d) images of the same flake as in (a). The step height between graphene and substrate is ~ 0.5 nm indicating mono-, or possibly bilayer graphene. The scale-bars in (c) and (d) are both 2 μm and the Z-scale in (c) is 5 nm.

Electrical measurements are performed both at room temperature and at 4 K. Figure 6.2 shows resistance as a function of voltage applied to the Nb-STO substrate acting as gate. A clear hysteresis is seen when sweeping the gate voltage, which is caused by switching of the ferroelectric state. The two peaks in the resistance are rather symmetric and well separated, in contrast to the previous works [130, 132]. The ratio between high- and low resistive states is larger than five. These are valuable characteristics when using the resistance of a graphene electrode as a read-out of the ferroelectric state.

The direction of hysteresis in Figure 6.2 is actually the opposite of that expected from the polarization field of the ferroelectric. This unusual resistance hysteresis is also seen for devices with graphene on ferroelectric $\text{Pb}(\text{Zr}_{0.2}\text{Ti}_{0.8})\text{O}_3$ (PZT) substrates [133]. In that case, it is believed the hysteresis is mainly caused by the dissociation and recombination of water molecules trapped in the interface between graphene and ferroelectric. There are however also differences. In Figure 6.2, the resistance

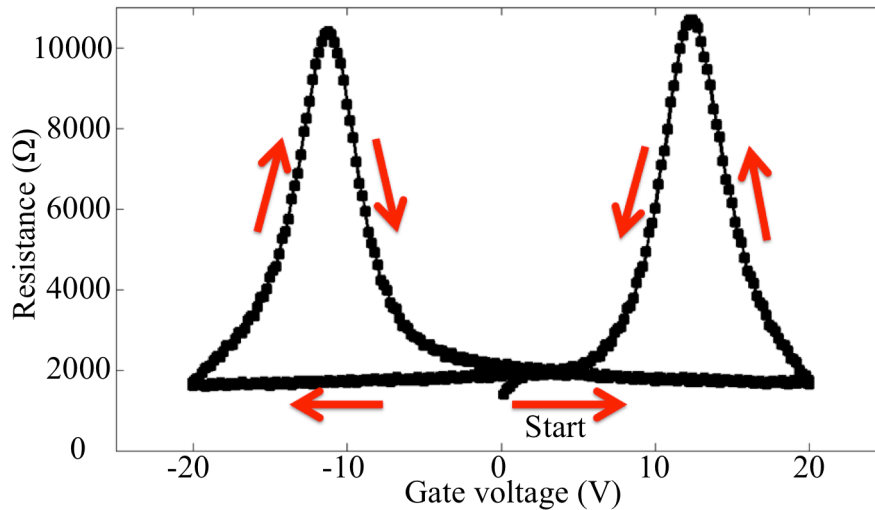


Figure 6.2: Resistance as a function of gate voltage for graphene on top of ferroelectric BSTO at 4 K. Two distinct resistance maxima are observed depending on the sweep direction of the gate voltage. The two peaks are symmetric and well separated. The hysteresis is opposite of that one would expect from a pure switching of the ferroelectric state.

saturates when applying only a few volts of different gate voltage compared to the Dirac voltages (two resistance peaks in this case due to the hysteresis). This combined with the well-separated peaks suggest that significant change in the charge carrier density is induced in contrast with the case of graphene on PZT.

6.3 Conclusions

Graphene on ferroelectric BSTO substrates exhibits a strong unusual resistance hysteresis, which might be utilized as a simple read-out in a graphene-ferroelectric hybrid memory device. The exact origin of the hysteresis remains unclear. It could be related to many phenomena including charge trapping in the oxide or on the surface of graphene, or the dynamics of surface bound water molecules. Further experiments on the dynamics of resistance states are needed.

In order to realize a memory device based on graphene on BSTO, device dimensions should be shrunk. Also, to decrease the operating voltage of this kind of device, a thinner ferroelectric film could be used.

7 Graphene bolometer

Graphene has been suggested as a sensor for a large number of applications. In this chapter we propose a graphene-based cold-electron bolometer for sensing microwave radiation. In Chapter 7.1, the idea behind the sensor is explained and the motivation on why to use graphene is presented. Chapter 7.2 describes the experimental layout and the measurement results. Finally, Chapter 7.3 contains conclusions and outlook.

7.1 Introduction

Graphene exhibits low mass, low charge carrier concentrations, and an extremely high surface-to-volume ratio making it interesting for many different kinds of sensors. In this chapter, graphene is proposed and examined as the absorber material in a cold-electron bolometer (CEB) [134, 135]. The CEB is a sensitive device for THz detection and temperature measurements at cryogenic temperatures. The sensitivity of such a device is strongly dependent on the absorber volume. The volume of graphene is ultimately low, making it a potentially interesting absorber material.

Basically, the CEB is a sensitive thermometer, which measures changes in temperature of a normal metal absorber by the non-linear characteristics of superconductor-insulator-normal metal (SIN) tunnel junctions. As a current is applied through the structure with two SIN junctions bridged by a normal metal strip, the voltage response will depend on the electron temperature of the absorber.

7.2 Experiment and results

The fabrication process consists of three lithography steps. Exfoliated graphene on standard SiO_2 / Si chips is patterned into rectangles of $5.5 \times 2.0 \mu\text{m}^2$. The silicon is not highly doped which makes it insulating at low temperature. This is to allow for microwave illumination of the device. Hence, there is no possibility of applying a gate voltage. In a second lithography step, two pillars with (SIN) tunnel junctions are deposited by thermal evaporation. The schematics of the device are shown in Figure 7.1(a). First a thin (1.5 nm) layer of Cr is deposited which (partially) oxidizes to form magnetic chromium oxide. This leads to suppression of superconductivity for the first Al layer, which is deposited on top (10 nm). Oxygen is let into the chamber to form a thin insulating layer of Al_2O_3 . Finally, a superconducting Al layer (70 nm) is

deposited and encapsulated by Pd (5 nm). The graphene bridges the two SIN junctions. In a third lithography step, 80 nm thick Al antenna leads connect to the junctions. An AFM phase image of the final devices is shown in Figure 7.1(b).

Electrical measurements are performed in two different cryostats. One is equipped with an optical window to enable optical response measurements down to 270 mK. The other is a cryogen-free dilution fridge with a base temperature of ~ 50 mK. Current is measured as a function of voltage for temperatures ranging from 50 mK to 350 mK as shown in Figure 7.2(a). Corresponding dynamical resistance $\partial V / \partial I$ is shown in Figure 7.2(b). For temperatures up to ~ 300 mK, the I-V is non-linear for voltages < 150 μ V. This roughly corresponds to the gap of Al (~ 200 μ V). The reason it is slightly lower is most likely due to over-heating of the device due to lack of filtering of the electrical wiring.

Figure 7.3(a) shows optical response measured using a 110 GHz source at 277 mK. The response is clearly visible but it is not normalized to responsivity due to

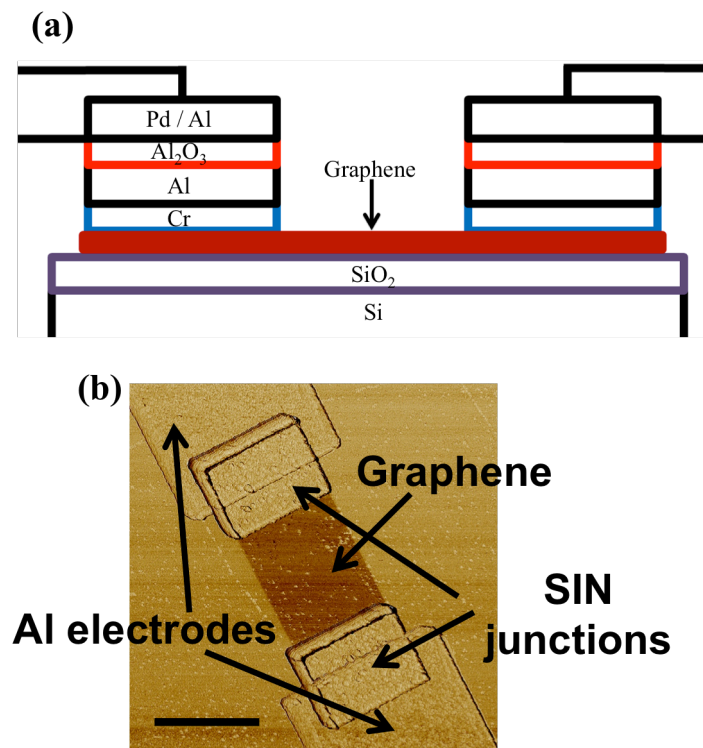


Figure 7.1: (a) Schematic side-view of the graphene-based CEB. Graphene is deposited on standard SiO_2 / Si substrates. A heterostructure of Al / Cr, Al_2O_3 , and Pd / Al is deposited using thermal evaporation. Superconductivity is suppressed in the bottom Al layer due to the thin Cr layer underneath. This layer (partially) oxidizes during deposition, forming magnetic chromium oxide. The Al_2O_3 layer is formed in situ by letting oxygen into the deposition chamber. Finally, a superconducting top Al layer is deposited and encapsulated by a thin layer of Pd. (b) AFM phase image of the fabricated device. The graphene bridges two SIN junctions connected by antenna electrodes. The scale-bar is 2 μm .

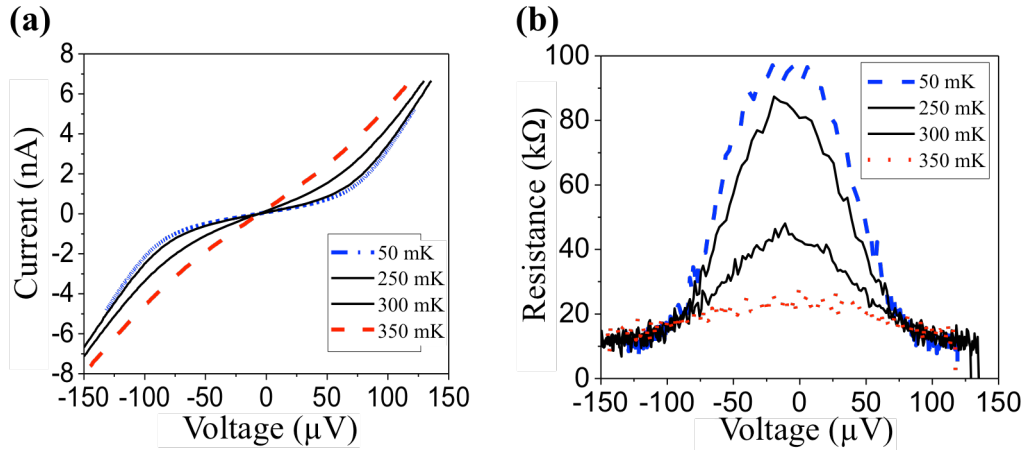


Figure 7.2: (a) Current as a function of voltage for a graphene-based bolometer in the temperature range from 50 mK to 350 mK and corresponding dynamical resistance (b). For temperatures lower than ~ 250 mK, the non-linear behavior saturates. The ratio between high- and low resistance regimes is ~ 10 .

lack of calibration of the microwave intensity. It is also possible to use the CEB as a pure thermometer. By measuring current-voltage characteristics for small temperature intervals (temperature as measured by the cryostat thermometer) the temperature responsivity of the device is obtained. This is shown in Figure 7.3(b). The maximum temperature responsivity of $\sim 0.4 \mu\text{V}/\text{mK}$ is found around 300 mK.

7.3 Conclusions

A graphene-based CEB with Al SIN tunnel junctions is realized and characterized. It shows optical response at 110 GHz. This was a first proof of principle experiment to investigate the feasibility of using graphene as absorber material. Several issues must be addressed in order to optimize the performance. The ratio between low- and high resistive states in the current-voltage characteristics is roughly two orders of magnitude lower than in state of the art devices with other normal metal absorbers.

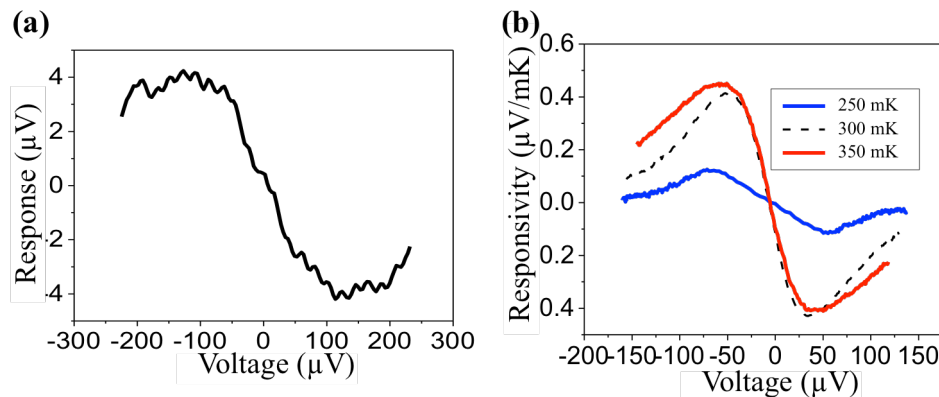


Figure 7.3: (a) Optical response for microwave radiation of frequency 110 GHz obtained at 277 mK. (b) Temperature responsivity at 250 mK, 300 mK, and 350 mK. The maximum responsivity of $\sim 0.4 \mu\text{V}/\text{mK}$ is obtained at approximately 300 mK.

The resistivity of graphene is higher than for most metals. This could be improved by intentional doping of the graphene and by fitting a gate electrode, which is sufficiently transparent to microwaves.

By utilizing a normal metal (Al / Cr) as part of SIN junction, the effective volume of the absorber (graphene plus the bottom layer of the SIN junctions) is probably greater than the volume of the graphene itself. While it is difficult to quantitatively estimate the effective volume, a CEB without any other normal metal is preferable. Al tunnel junctions can be made directly to graphene, opening up new possibilities of making the ultimate low volume CEB [136].

8 Aharonov-Bohm effect in graphene

In this chapter, the quantum mechanical Aharonov-Bohm effect is studied in graphene. Chapter 8.1 gives a background to the experiment and the idea of using “mirrors” to enhance the coherence of the system. In Chapter 8.2, the experimental results shown where indeed the mirrors make higher order Aharonov-Bohm signals visible. Finally, Chapter 8.3 provides conclusions.

8.1 Introduction

Electrons behave quantum-mechanically. If they can retain their quantum mechanical phase on the length scale of a measured device, they behave coherently and interfere leading to changes in the device properties. Quantum-mechanical interference phenomena in graphene, such as the Aharonov-Bohm effect, were studied earlier [137-142]. Typically only the first harmonic of oscillations is seen in experiments on graphene. Sometimes, usually at high magnetic fields, also the second harmonic signal is seen but with low visibility. One way to improve the coherence of the system is to deposit metal mirrors to confine the charge carriers to the ring. The mirrors can be made from either normal metals or by a superconducting material. To see the effect of mirrors on a graphene nanoring structure, we study samples with both ordinary metal (Au) and superconducting (Al) mirrors as well as samples without mirrors [143]. Some of these devices are even fit to the same graphene flake to make all the other parameters as similar as possible.

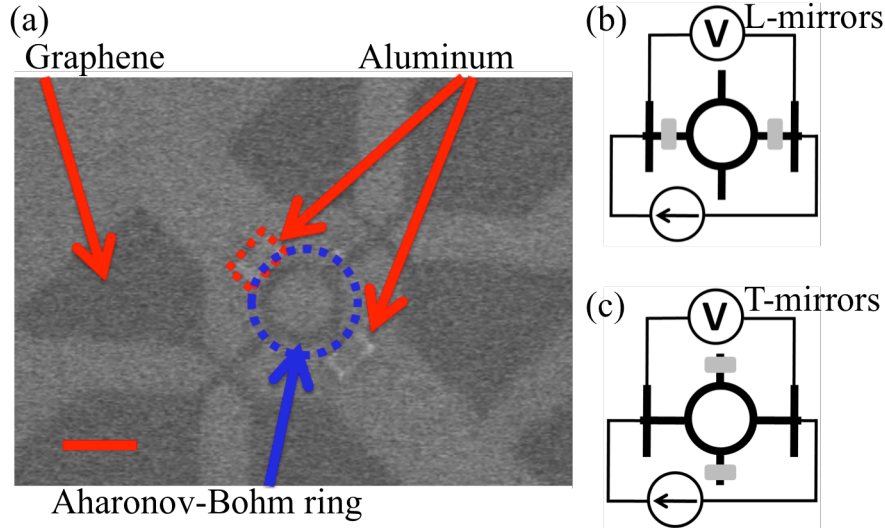


Figure 8.1: (a) SEM image of a graphene Aharonov-Bohm device after patterning. The blue, dotted circle outlines the graphene ring. Aluminum mirrors are deposited on the perimeter of the ring as indicated by the arrows. The scale-bar is $1\ \mu\text{m}$. (b) and (c) Illustrations of longitudinal- (L) and transverse (T) mirror configurations, respectively.

8.2 Experiment and results

Devices are prepared with no mirrors, mirrors in the transverse direction- (T-mirrors), or mirrors in the longitudinal direction (L-mirrors) of the current path. A SEM micrograph of a device with aluminum mirrors in the T-mirror configuration is shown in Figure 8.1(a). Darker areas are graphene. The ring diameter is $1.0\ \mu\text{m}$ and the width of the current path is $150\ \text{nm}$. The inner- and outer diameters of the ring give a range for the first harmonic of Aharonov-Bohm oscillations of $140\text{-}250\ 1/T$. In Figure 8.1(b) and (c), L- and T-mirror configurations are shown, respectively.

The resistance is measured as a function of the magnetic field for a set of temperatures ranging from the base temperature of $20\ \text{mK}$ to $1590\ \text{mK}$. Magnetic fields up to a few tesla are applied. For such a narrow graphene channel at low temperature, UCFs are dominant and no IQHE is seen in this regime. As well as low temperature, a low voltage across the samples is needed to avoid smearing of the quantum effects. For this reason, the voltage is kept well below the thermal limit, that is $V \ll k_B T / e$.

The Dirac voltage of these devices is typically at plus few tens of volts. Hence, the graphene charge carrier concentration is high when sweeping the magnetic field at $V_g = 0$.

Figure 8.2(a) shows a typical measurement of resistance as a function of magnetic field for a sample with L-mirrors (made of Al) at $17\ \text{mK}$. On top of large UCFs, a small periodic signal is seen. To distinguish between the aperiodic UCFs and the periodic Aharonov-Bohm oscillations, FFT is performed. To enhance visibility by removing the overall magnetoresistance, a running average filter is utilized prior to

FFT. The averaging window is chosen to be 5 mT giving the best result, but a similar result is obtained using other values. Figure 8.2(b) and (c) show typical FFT data for samples with T-mirrors and L-mirrors, respectively. For both types of sample, the first harmonic (h/e) is clearly visible. For T-mirror samples, only a weak second order harmonic signal is observed, indicating limited coherence of the system. For L-mirror samples on the other hand, both first- and second harmonic signals are clearly visible. Even the third harmonic can be seen, proving significantly increased coherence.

The phase coherence length l_ϕ of the system is estimated independently from both weak localization and the Einstein relation to be $\sim 1\text{-}2\ \mu\text{m}$, which is similar to the diameter of the ring.

The third order oscillations were not seen earlier. Also, even the second harmonic signal was only seen at high magnetic fields ($\approx 4\ T$). In our experiments we observe higher order peaks at both low and high magnetic fields. There are two fundamental differences in our experiment. First, the mirrors are expected to improve coherence by confining charge carriers to the ring. We can see a clear difference between the two mirror configurations, indicating that they play a major role. Second, the temperature in this experiment is significantly lower than in those previous. Indeed, by increasing the temperature moderately to 78 mK, the third harmonic peak disappears while the second harmonic signal turns weak, even for a sample with L-mirrors. FFT data for a L-mirror sample at temperatures from 17 mK to 1590 mK

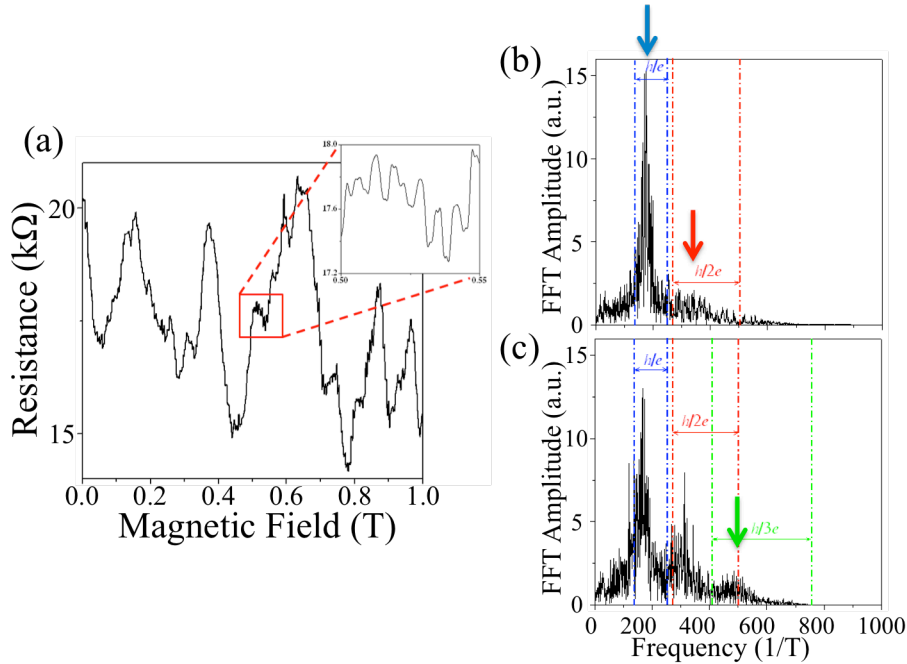


Figure 8.2: (a) Resistance as a function of magnetic field for a sample with L-mirrors measured at 17 mK. Small, periodic oscillations are seen on top of the larger aperiodic UCFs. The inset shows a zoom-in to further visualize the periodic oscillations. (b) and (c) FFT spectra after filtering for T- and L-mirror samples, respectively. The dashed lines correspond to theoretical values for the first (blue), second (red), and third (green) order oscillations determined from the inner- and outer diameters of the ring. The arrows point at the peak positions.

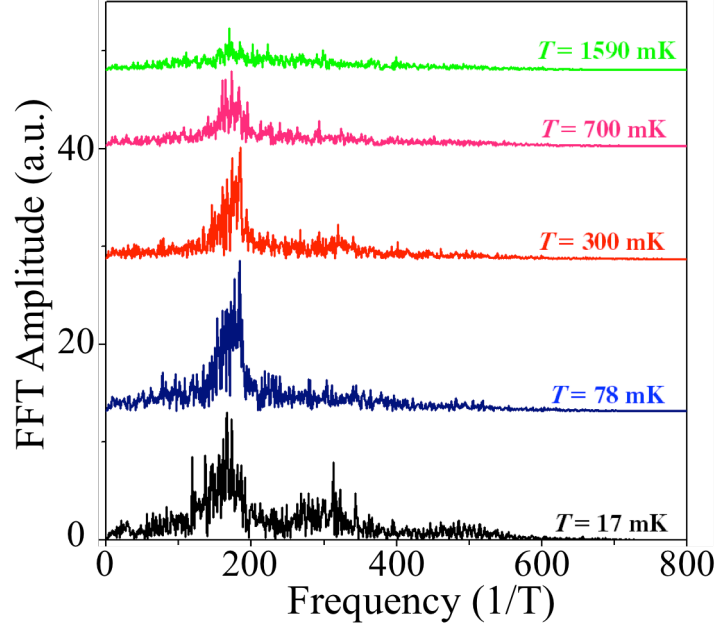


Figure 8.3: Temperature dependence of FFT spectrum for a graphene Aharonov-Bohm device with L-mirror configuration. At the base temperature of 17 mK, first-, second-, and third order Aharonov-Bohm oscillations are observed. Already at 78 mK, the second order oscillations are difficult to see. At the highest measured temperature of 1590 mK, only a weak first order signal is observed. Curves are shifted along the ordinate for clarity.

are shown in Figure 8.3. At base temperature, all three harmonic signals are visible. At elevated temperature, the third harmonic peak vanishes and at the highest measured temperature only a weak first harmonic signal is observed.

It should be noted that samples have so far been fabricated using different graphene flakes. To study the effects of the mirrors more accurately, samples with and without mirrors fabricated on the same graphene flake are studied. Sadly, these samples turned out to be of lower quality than the previous ones (in terms of mobility, phase coherence, and charge neutrality) and the third order oscillations were not observed. However, a significant improvement of the first order signal is observed when L-mirrors were present. This is true for samples with both Al and Au/Ti mirrors. For samples with T-mirrors, however, no improvement is seen independent of mirror material.

8.3 Conclusions

It is possible to increase the visibility of Aharonov-Bohm oscillations in graphene nanorings by depositing metal mirrors in the current path. These can be either metallic or superconducting and serve the purpose of confining charge carriers to the ring. A strong increase in the visibility of higher order harmonic signals is observed in samples with mirrors in the current path. For samples with mirrors in the transverse direction no improvement is observed. For L-mirror samples, up to third order harmonic oscillations are observed at the base temperature of 17 mK.

Appendix A: Recipes for sample fabrication

EBL graphene etch recipe

- Substrate cleaning, typically acetone and isopropanol
- Spin coat ZEP520A, 4 krpm
- Soft bake of resist, 5 min at 160 °C
- EBL exposure, 300 $\mu\text{C}/\text{cm}^2$
- Develop in anisole 60 s, clean in isopropanol
- Etch in oxygen plasma, 10 s at 50 W
- Remove all resist in 1165 remove and clean in acetone and isopropanol

EBL lift-off recipe

- Substrate cleaning, typically acetone and isopropanol
- Spin coat copolymer (EL10), 4 krpm
- Soft bake of resist, 5 min at 160 °C
- Spin coat PMMA (A2), 4 krpm
- Soft bake of resist, 5 min at 160 °C
- EBL exposure, 300 $\mu\text{C}/\text{cm}^2$
- Develop in isobutyl ketone:isopropanol 1:1 90 s, clean in isopropanol
- Metal deposition followed by lift-off in 1165 remover
- Clean in acetone and isopropanol

Acknowledgements

First of all, I thank my supervisor August Yurgens for giving me the chance to work on the exciting topic of graphene. I am especially thankful for all faith and responsibility that I have received, in good and bad times. Thanks for always finding the time to provide your guidance regarding all different kinds of questions.

I am very grateful to my co-supervisor, Jie Sun, for helping me a lot in understanding the somewhat peculiar world of science. Thanks also for all the nice discussions about almost all different aspects of life. I am sure we will share many more great times together!

I wish to express my gratitude to my other co-supervisor Dag Winkler and my examiner Mikael Fogelström for their advice on how to work in research. I will try to follow it.

Youngwoo Nam, thanks for all the nice times in different labs and thanks a lot for showing me Korea, an experience to remember to say the least.

I would like to thank Niklas Lindahl and Johannes Svensson from Gothenburg University for enlightening collaborations. Both of you share an enthusiasm for Physics which is truly remarkable.

I am very grateful for the help from Tim Booth and Peter Bøggild from DTU, and from Olof Bäcké, Markus Löffler, and Eva Olsson from Chalmers, regarding TEM analysis.

Thanks a lot Alexey Kalabukhov, for all your advice, teaching, patience, and exemplary working pace. I learned a lot.

Thanks to my office mate Riccardo Arpaia, for all the fun times. Science and food, in perfect harmony.

I am very grateful to Marie Fredriksson, Debora Perlheden, and Ann-Marie Frykestig for the administrative support as well as to Lars Jönsson and Staffan Persson who create wonders in the machine shop.

Thanks also to the clean room staff for all the process support and training.

I thank Philip Krantz, Samuel Lara Avila, Mikhail Tarasov, Sumedh Mahashabde, André Dankert, Shahid Nawaz, Martin Gustafsson, Arsalan Pourkabirian, Simon Abay, Tord Claeson, Fredrik Öisjöen, David Gustafsson, Per Delsing, Seckin Kintas, Io-Chun Hoi, Sebastian de Graaf, Sergey Kubatkin, Saroj Dash, Michaël Simoen, Thomas Yager, Arseniy Lartsev, Marco Arzeo, Pier Paolo Aurino, Floriana Lombardi, Sophie Charpentier, Leonid Kuzmin,

Kyle Sundqvist, and all other past and present QDP staff who make this such an inspiring place to work.

Finally I would like to thank all my friends and family for their support over the years. I couldn't do without it.

Bibliography

- [1] A. J. Van Bommel, J. E. Crombeen, and A. Van Tooren, "LEED and Auger electron observations of the SiC(0001) surface", *Surf Sci* vol. **48**, pp 463-472, 1975.
- [2] R. Rosei, M. De Crescenzi, F. Sette, C. Quaresima, A. Savoia, and P. Perfetti, "Structure of graphitic carbon on Ni(111): A surface extended-energy-loss fine-structure study", *Phys Rev B* vol. **28**, pp 1161-1164, 1983.
- [3] K. S. Novoselov, A. K. Geim, S. V. Morozov, D. Jiang, Y. Zhang, S. V. Dubonos, I. V. Grigorieva, and A. A. Firsov, "Electric field effect in atomically thin carbon films", *Science* vol. **306**, pp 666-669, 2004.
- [4] K. S. Novoselov, D. Jiang, F. Schedin, T. J. Booth, V. V. Khotkevich, S. V. Morozov, and A. K. Geim, "Two-dimensional atomic crystals", *PNAS* vol. **102**, pp 10451-10453, 2005.
- [5] Y. B. Zhang, Y. W. Tan, H. L. Stormer, and P. Kim, "Experimental observation of the quantum Hall effect and Berry's phase in graphene", *Nature* vol. **438**, pp 201-204, 2005.
- [6] R. E. Peierls, "Quelques propriétés typiques des corps solides", *Ann. I. H. Poincare* vol. **5**, pp 177-222, 1935.
- [7] L. D. Landau, "Zur Theorie der phasenumwandlungen II", *Phys. Z. Sowjetunion* vol. **11**, pp 26-35, 1937.
- [8] N. D. Mermin, "Crystalline order in two dimensions", *Phys Rev* vol. **176**, pp 250-254, 1968.
- [9] A. Barth, and W. Marx, "Graphene - a rising star in view of scientometrics", arXiv:0808.3320v3, 2008.
- [10] M. D. Stoller, S. J. Park, Y. W. Zhu, J. H. An, and R. S. Ruoff, "Graphene-based ultracapacitors", *Nano Lett* vol. **8**, pp 3498-3502, 2008.
- [11] P. L. McEuen, J. S. Bunch, S. S. Verbridge, J. S. Alden, A. M. van der Zande, J. M. Parpia, and H. G. Craighead, "Impermeable atomic membranes from graphene sheets", *Nano Lett* vol. **8**, pp 2458-2462, 2008.
- [12] C. Lee, X. Wei, J. W. Kysar, and J. Hone, "Measurement of the elastic properties and intrinsic strength of monolayer graphene", *Science* vol. **321**, pp 385-388, 2008.

- [13] A. S. Mayorov, R. V. Gorbachev, S. V. Morozov, L. Britnell, R. Jalil, L. A. Ponomarenko, P. Blake, K. S. Novoselov, K. Watanabe, T. Taniguchi, and A. K. Geim, "Micrometer-scale ballistic transport in encapsulated graphene at room temperature", *Nano Lett* vol. **11**, pp 2396-2399, 2011.
- [14] A. A. Balandin, S. Ghosh, W. Z. Bao, I. Calizo, D. Teweldebrhan, F. Miao, and C. N. Lau, "Superior thermal conductivity of single-layer graphene", *Nano Lett* vol. **8**, pp 902-907, 2008.
- [15] R. R. Nair, P. Blake, A. N. Grigorenko, K. S. Novoselov, T. J. Booth, T. Stauber, N. M. R. Peres, and A. K. Geim, "Fine structure constant defines visual transparency of graphene", *Science* vol. **320**, pp 1308-1308, 2008.
- [16] F. Bonaccorso, Z. Sun, T. Hasan, and A. C. Ferrari, "Graphene photonics and optoelectronics", *Nature Photon* vol. **4**, pp 611-622, 2010.
- [17] M. Liu, X. Yin, and X. Zhang, "Double-layer graphene optical modulator", *Nano Lett* vol. **12**, pp 1482-1485, 2012.
- [18] X. Huang, X. Qi, F. Boey, and H. Zhang, "Graphene-based composites", *Chem Soc Rev* vol. **41**, pp 666-686, 2012.
- [19] S. Bae, H. Kim, Y. Lee, X. F. Xu, J. S. Park, Y. Zheng, J. Balakrishnan, T. Lei, H. R. Kim, Y. I. Song, Y. J. Kim, K. S. Kim, B. Ozyilmaz, J. H. Ahn, B. H. Hong, and S. Iijima, "Roll-to-roll production of 30-inch graphene films for transparent electrodes", *Nature Nanotech* vol. **5**, pp 574-578, 2010.
- [20] K. S. Kim, Y. Zhao, H. Jang, S. Y. Lee, J. M. Kim, K. S. Kim, J. H. Ahn, P. Kim, J. Y. Choi, and B. H. Hong, "Large-scale pattern growth of graphene films for stretchable transparent electrodes", *Nature* vol. **457**, pp 706-710, 2009.
- [21] L. G. De Arco, Y. Zhang, C. W. Schlenker, K. Ryu, M. E. Thompson, and C. W. Zhou, "Continuous, highly flexible, and transparent graphene films by chemical vapor deposition for organic photovoltaics", *ACS Nano* vol. **4**, pp 2865-2873, 2010.
- [22] M. C. Lemme, F. H. L. Koppens, A. L. Falk, M. S. Rudner, H. Park, L. S. Levitov, and C. M. Marcus, "Gate-activated photoresponse in a graphene p-n junction", *Nano Lett* vol. **11**, pp 4134-4137, 2011.
- [23] S. Rumyantsev, G. Liu, M. S. Shur, R. A. Potyrailo, and A. A. Balandin, "Selective gas sensing with a single pristine graphene transistor", *Nano Lett*, 2012.
- [24] G. Konstantatos, M. Badioli, L. Gaudreau, J. Osmond, M. Bernechea, F. P. G. de Arquer, F. Gatti, and F. H. L. Koppens, "Hybrid graphene-quantum dot phototransistors with ultrahigh gain", *Nature Nanotech* advance online publication, 2012.
- [25] G. E. Moore, "Cramming more components onto integrated circuits", *Electronics* vol. **38**, 1965.
- [26] G. E. Moore, "Progress in digital integrated electronics", *IEEE IEDM Tech Dig* vol. **21**, pp 11-13, 1975.
- [27] Y. Q. Wu, Y. M. Lin, A. A. Bol, K. A. Jenkins, F. N. Xia, D. B. Farmer, Y. Zhu, and P. Avouris, "High-frequency, scaled graphene transistors on diamond-like carbon", *Nature* vol. **472**, pp 74-78, 2011.

- [28] L. Liao, J. W. Bai, R. Cheng, Y. C. Lin, S. Jiang, Y. Q. Qu, Y. Huang, and X. F. Duan, "Sub-100 nm channel length graphene transistors", *Nano Lett* vol. **10**, pp 3952-3956, 2010.
- [29] F. Schwierz, "Graphene transistors", *Nature Nanotech* vol. **5**, pp 487-496, 2010.
- [30] Y. M. Lin, A. Valdes-Garcia, S. J. Han, D. B. Farmer, I. Meric, Y. N. Sun, Y. Q. Wu, C. Dimitrakopoulos, A. Grill, P. Avouris, and K. A. Jenkins, "Wafer-scale graphene integrated circuit", *Science* vol. **332**, pp 1294-1297, 2011.
- [31] J. Xiao, D. Mei, X. Li, W. Xu, D. Wang, G. L. Graff, W. D. Bennett, Z. Nie, L. V. Saraf, I. A. Aksay, J. Liu, and J.-G. Zhang, "Hierarchically porous graphene as a lithium-air battery electrode", *Nano Lett* vol. **11**, pp 5071-5078, 2011.
- [32] X. Zhao, C. M. Hayner, M. C. Kung, and H. H. Kung, "In-plane vacancy-enabled high-power Si-graphene composite electrode for lithium-ion batteries", *Adv Energy Mater* vol. **1**, pp 1079-1084, 2011.
- [33] P. Matyba, H. Yamaguchi, M. Chhowalla, N. D. Robinson, and L. Edman, "Flexible and metal-free light-emitting electrochemical cells based on graphene and PEDOT-PSS as the electrode materials", *ACS Nano* vol. **5**, pp 574-580, 2010.
- [34] J. Hou, Y. Shao, M. W. Ellis, R. B. Moore, and B. Yi, "Graphene-based electrochemical energy conversion and storage: fuel cells, supercapacitors and lithium ion batteries", *Phys Chem Chem Phys* vol. **13**, pp 15384-15402, 2011.
- [35] "An analysis of worldwide patent filings relating to graphene", Patent Informatics Team, Intellectual Property Office, Concept House, Cardiff Rd, Newport, South Wales, NP10 8QQ, UK, 2011.
- [36] H. Kroemer, "Nano-whatever: Do we really know where we are heading?", *Phys Status Solidi A* vol. **202**, pp 957-964, 2005.
- [37] R. H. Baughman, A. A. Zakhidov, and W. A. de Heer, "Carbon nanotubes - the route toward applications", *Science* vol. **297**, pp 787-792, 2002.
- [38] Y. Lifshitz, "Diamond-like carbon - present status", *Diam Relat Mater* vol. **8**, pp 1659-1676, 1999.
- [39] H. C. Tsai, and D. B. Bogy, "Characterization of diamond-like carbon-films and their application as overcoats on thin-film media for magnetic recording", *J Vac Sci Technol A* vol. **5**, pp 3287-3312, 1987.
- [40] A. Schinwald, F. A. Murphy, A. Jones, W. MacNee, and K. Donaldson, "Graphene-based nanoplatelets: A new risk to the respiratory system as a consequence of their unusual aerodynamic properties", *ACS Nano* vol. **6**, pp 736-746, 2012.
- [41] K. Donaldson, and C. A. Poland, "Nanotoxicology new insights into nanotubes", *Nature Nanotech* vol. **4**, pp 708-710, 2009.
- [42] K. Welsher, S. P. Sherlock, and H. J. Dai, "Deep-tissue anatomical imaging of mice using carbon nanotube fluorophores in the second near-infrared window", *PNAS* vol. **108**, pp 8943-8948, 2011.

- [43] A. K. Geim, and K. S. Novoselov, "The rise of graphene", *Nature Mater* vol. **6**, pp 183-191, 2007.
- [44] A. H. Castro Neto, F. Guinea, N. M. R. Peres, K. S. Novoselov, and A. K. Geim, "The electronic properties of graphene", *Rev Mod Phys* vol. **81**, pp 109-162, 2009.
- [45] M. I. Katsnelson, K. S. Novoselov, and A. K. Geim, "Chiral tunnelling and the Klein paradox in graphene", *Nature Phys* vol. **2**, pp 620-625, 2006.
- [46] S. Kim, J. Nah, I. Jo, D. Shahrjerdi, L. Colombo, Z. Yao, E. Tutuc, and S. K. Banerjee, "Realization of a high mobility dual-gated graphene field-effect transistor with Al₂O₃ dielectric", *Appl Phys Lett* vol. **94**, p. 062107, 2009.
- [47] M. Shayegan, "Flatland electrons in high magnetic fields", arXiv:cond-mat/0505520v1, 2005.
- [48] K. v. Klitzing, G. Dorda, and M. Pepper, "New method for high-accuracy determination of the fine-structure constant based on quantized Hall resistance", *Phys Rev Lett* vol. **45**, pp 494-497, 1980.
- [49] A. Tzalenchuk, S. Lara-Avila, A. Kalaboukhov, S. Paolillo, M. Syvajarvi, R. Yakimova, O. Kazakova, T. J. B. M. Janssen, V. Fal'ko, and S. Kubatkin, "Towards a quantum resistance standard based on epitaxial graphene", *Nature Nanotech* vol. **5**, pp 186-189, 2010.
- [50] C. Kittel, "Introduction to solid state physics", pp 543-544, (Wiley, 2005),
- [51] V. T. Petrashov, V. N. Antonov, P. Delsing, and R. Claeson, "Phase memory effects in mesoscopic rings with superconducting "mirrors"", *Phys Rev Lett* vol. **70**, pp 347-350, 1993.
- [52] V. T. Petrashov, V. N. Antonov, R. S. Shaikhaidarov, S. V. Maksimov, P. Meeson, R. Souhami, and M. Springford, "'Giant" Aharonov-Bohm effect in mesoscopic silver rings with bismuth electrodes", *Europhys Lett* vol. **34**, pp 593-598, 1996.
- [53] C. W. J. Beenakker, and H. Vanhouten, "Quantum transport in semiconductor nanostructures", *Solid State Phys* vol. **44**, pp 1-228, 1991.
- [54] P. Blake, E. W. Hill, A. H. C. Neto, K. S. Novoselov, D. Jiang, R. Yang, T. J. Booth, and A. K. Geim, "Making graphene visible", *Appl Phys Lett* vol. **91**, p. 063124, 2007.
- [55] C. Virojanadara, M. Syvajarvi, R. Yakimova, L. I. Johansson, A. A. Zakharov, and T. Balasubramanian, "Homogeneous large-area graphene layer growth on 6H-SiC(0001)", *Phys Rev B* vol. **78**, 2008.
- [56] Y. Hernandez, V. Nicolosi, M. Lotya, F. M. Blighe, Z. Y. Sun, S. De, I. T. McGovern, B. Holland, M. Byrne, Y. K. Gun'ko, J. J. Boland, P. Niraj, G. Duesberg, S. Krishnamurthy, R. Goodhue, J. Hutchison, V. Scardaci, A. C. Ferrari, and J. N. Coleman, "High-yield production of graphene by liquid-phase exfoliation of graphite", *Nature Nanotech* vol. **3**, pp 563-568, 2008.
- [57] G. Eda, G. Fanchini, and M. Chhowalla, "Large-area ultrathin films of reduced graphene oxide as a transparent and flexible electronic material", *Nature Nanotech* vol. **3**, pp 270-274, 2008.
- [58] J. M. Cai, P. Ruffieux, R. Jaafar, M. Bieri, T. Braun, S. Blankenburg, M. Muoth, A. P. Seitsonen, M. Saleh, X. L. Feng, K. Mullen, and R. Fasel, "Atomically precise bottom-up fabrication of graphene nanoribbons", *Nature* vol. **466**, pp 470-473, 2010.

- [59] I. Vlassioux, M. Regmi, P. F. Fulvio, S. Dai, P. Datskos, G. Eres, and S. Smirnov, "Role of hydrogen in chemical vapor deposition growth of large single-crystal graphene", *ACS Nano* vol. **5**, pp 6069-6076, 2011.
- [60] A. N. Obraztsov, E. A. Obraztsova, A. V. Tyurnina, and A. A. Zolotukhin, "Chemical vapor deposition of thin graphite films of nanometer thickness", *Carbon* vol. **45**, pp 2017-2021, 2007.
- [61] Y. Zhang, L. Gomez, F. N. Ishikawa, A. Madaria, K. Ryu, C. A. Wang, A. Badmaev, and C. W. Zhou, "Comparison of graphene growth on single-crystalline and polycrystalline Ni by chemical vapor deposition", *J Phys Chem Lett* vol. **1**, pp 3101-3107, 2010.
- [62] J. F. Colomer, C. Stephan, S. Lefrant, G. Van Tendeloo, I. Willems, Z. Konya, A. Fonseca, C. Laurent, and J. B. Nagy, "Large-scale synthesis of single-wall carbon nanotubes by catalytic chemical vapor deposition (CCVD) method", *Chem Phys Lett* vol. **317**, pp 83-89, 2000.
- [63] X. S. Li, W. W. Cai, J. H. An, S. Kim, J. Nah, D. X. Yang, R. Piner, A. Velamakanni, I. Jung, E. Tutuc, S. K. Banerjee, L. Colombo, and R. S. Ruoff, "Large-area synthesis of high-quality and uniform graphene films on copper foils", *Science* vol. **324**, pp 1312-1314, 2009.
- [64] C.-a. Di, D. Wei, G. Yu, Y. Liu, Y. Guo, and D. Zhu, "Patterned graphene as source/drain electrodes for bottom-contact organic field-effect transistors", *Adv Mater* vol. **20**, pp 3289-3293, 2008.
- [65] S. Nie, W. Wu, S. Xing, Q. Yu, S.-s. Pei, and K. McCarty, "Growth from below: Bilayer graphene on copper by chemical vapor deposition", arXiv:1202.1031v1, 2012.
- [66] S. Bhaviripudi, X. T. Jia, M. S. Dresselhaus, and J. Kong, "Role of kinetic factors in chemical vapor deposition synthesis of uniform large area graphene using copper catalyst", *Nano Lett* vol. **10**, pp 4128-4133, 2010.
- [67] W. Gannett, W. Regan, K. Watanabe, T. Taniguchi, M. F. Crommie, and A. Zettl, "Boron nitride substrates for high mobility chemical vapor deposited graphene", *Appl Phys Lett* vol. **98**, 2011.
- [68] J. Sun, N. Lindvall, M. Cole, K. Angel, T. Wang, K. Teo, D. Chua, J. Liu, and A. Yurgens, "Low partial pressure chemical vapor deposition of graphene on copper", *IEEE Trans Nanotechnol* vol. **11**, pp 255-260, 2012.
- [69] L. Tao, J. Lee, H. Chou, M. Holt, R. S. Ruoff, and D. Akinwande, "Synthesis of high quality monolayer graphene at reduced temperature on hydrogen-enriched evaporated copper (111) films", *ACS Nano* vol. **6**, pp 2319-2325, 2012.
- [70] A. Ismach, C. Druzgalski, S. Penwell, A. Schwartzberg, M. Zheng, A. Javey, J. Bokor, and Y. G. Zhang, "Direct chemical vapor deposition of graphene on dielectric surfaces", *Nano Lett* vol. **10**, pp 1542-1548, 2010.
- [71] G. I. Kozlov, and V. G. Knorre, "Single-pulse shock tube studies on the kinetics of the thermal decomposition of methane", *Combustion and Flame* vol. **6**, pp 253-263, 1962.
- [72] H. L. Cao, Q. K. Yu, L. A. Jauregui, J. Tian, W. Wu, Z. Liu, R. Jalilian, D. K. Benjamin, Z. Jiang, J. Bao, S. S. Pei, and Y. P. Chen, "Electronic transport in chemical vapor deposited graphene synthesized on Cu: Quantum Hall effect and weak localization", *Appl Phys Lett* vol. **96**, 2010.

- [73] Y. Lee, S. Bae, H. Jang, S. Jang, S. E. Zhu, S. H. Sim, Y. I. Song, B. H. Hong, and J. H. Ahn, "Wafer-scale synthesis and transfer of graphene films", *Nano Lett* vol. **10**, pp 490-493, 2010.
- [74] X. S. Li, C. W. Magnuson, A. Venugopal, J. H. An, J. W. Suk, B. Y. Han, M. Borysiak, W. W. Cai, A. Velamakanni, Y. W. Zhu, L. F. Fu, E. M. Vogel, E. Voelkl, L. Colombo, and R. S. Ruoff, "Graphene films with large domain size by a two-step chemical vapor deposition process", *Nano Lett* vol. **10**, pp 4328-4334, 2010.
- [75] E. H. Lock, M. Baraket, M. Laskoski, S. P. Mulvaney, W. K. Lee, P. E. Sheehan, D. R. Hines, J. T. Robinson, J. Tosado, M. S. Fuhrer, S. C. Hernandez, and S. G. Walton, "High-quality uniform dry transfer of graphene to polymers", *Nano Lett* vol. **12**, pp 102-107, 2012.
- [76] J. Sun, N. Lindvall, M. T. Cole, T. Wang, T. J. Booth, P. Boggild, K. B. K. Teo, J. Liu, and A. Yurgens, "Controllable chemical vapor deposition of large area uniform nanocrystalline graphene directly on silicon dioxide", *J Appl Phys* vol. **111**, p. 044103, 2012.
- [77] J. Sun, M. T. Cole, N. Lindvall, K. B. K. Teo, and A. Yurgens, "Noncatalytic chemical vapor deposition of graphene on high-temperature substrates for transparent electrodes", *Appl Phys Lett* vol. **100**, p. 022102, 2012.
- [78] J. Sun, N. Lindvall, M. T. Cole, K. B. K. Teo, and A. Yurgens, "Large-area uniform graphene-like thin films grown by chemical vapor deposition directly on silicon nitride", *Appl Phys Lett* vol. **98**, p. 252107, 2011.
- [79] M. A. Fanton, J. A. Robinson, C. Puls, Y. Liu, M. J. Hollander, B. E. Weiland, M. LaBella, K. Trumbull, R. Kasarda, C. Howsare, J. Stitt, and D. W. Snyder, "Characterization of graphene films and transistors grown on sapphire by metal-free chemical vapor deposition", *ACS Nano* vol. **5**, pp 8062-8069, 2011.
- [80] Y. Miyasaka, A. Nakamura, and J. Temmyo, "Graphite thin films consisting of nanograins of multilayer graphene on sapphire substrates directly grown by alcohol chemical vapor deposition", *Jpn J Appl Phys* vol. **50**, p. 04DH12.
- [81] D. Wei, Y. Liu, H. Zhang, L. Huang, B. Wu, J. Chen, and G. Yu, "Scalable synthesis of few-layer graphene ribbons with controlled morphologies by a template method and their applications in nanoelectromechanical switches", *J Am Chem Soc* vol. **131**, pp 11147-11154, 2009.
- [82] M. H. Rummeli, A. Bachmatiuk, A. Scott, F. Börrnert, J. H. Warner, V. Hoffman, J.-H. Lin, G. Cuniberti, and B. Büchner, "Direct low-temperature nanographene CVD synthesis over a dielectric insulator", *ACS Nano* vol. **4**, pp 4206-4210, 2010.
- [83] X. Ding, G. Ding, X. Xie, F. Huang, and M. Jiang, "Direct growth of few layer graphene on hexagonal boron nitride by chemical vapor deposition", *Carbon* vol. **49**, pp 2522-2525, 2011.
- [84] J. Hofrichter, B. N. Szafraneck, M. Otto, T. J. Echtermeyer, M. Baus, A. Majerus, V. Geringer, M. Ramsteiner, and H. Kurz, "Synthesis of graphene on silicon dioxide by a solid carbon source", *Nano Lett* vol. **10**, pp 36-42, 2010.
- [85] A. Oya, and H. Marsh, "Phenomena of catalytic graphitization", *J Mater Sci* vol. **17**, pp 309-322, 1982.
- [86] M. S. Dresselhaus, A. Jorio, M. Hofmann, G. Dresselhaus, and R. Saito, "Perspectives on carbon nanotubes and graphene Raman spectroscopy", *Nano Lett* vol. **10**, pp 751-758, 2010.

- [87] A. C. Ferrari, "Raman spectroscopy of graphene and graphite: Disorder, electron-phonon coupling, doping and nonadiabatic effects", *Solid State Commun* vol. **143**, pp 47-57, 2007.
- [88] A. C. Ferrari, J. C. Meyer, V. Scardaci, C. Casiraghi, M. Lazzeri, F. Mauri, S. Piscanec, D. Jiang, K. S. Novoselov, S. Roth, and A. K. Geim, "Raman spectrum of graphene and graphene layers", *Phys Rev Lett* vol. **97**, 2006.
- [89] G. Bergmann, "Weak localization in thin-films - a time-of-flight experiment with conduction electrons", *Phys Rep* vol. **107**, pp 1-58, 1984.
- [90] F. V. Tikhonenko, D. W. Horsell, R. V. Gorbachev, and A. K. Savchenko, "Weak localization in graphene flakes", *Phys Rev Lett* vol. **100**, 2008.
- [91] Y. Wang, and J. J. Santiago-Aviles, "Large negative magnetoresistance and strong localization in highly disordered electrospun pregraphitic carbon nanofiber", *Appl Phys Lett* vol. **89**, 2006.
- [92] X. Zhang, Q. Z. Xue, and D. D. Zhu, "Positive and negative linear magnetoresistance of graphite", *Phys Lett A* vol. **320**, pp 471-477, 2004.
- [93] A. Faisst, and H. von Lohneysen, "Electrical resistance and magnetoresistance of pyrocarbon at low temperatures in fields up to 14 Tesla", *Carbon* vol. **40**, pp 321-327, 2002.
- [94] V. I. Fal'ko, K. Kechedzhi, E. McCann, B. L. Altshuler, H. Suzuura, and T. Ando, "Weak localization in graphene", *Solid State Commun* vol. **143**, pp 33-38, 2007.
- [95] M. A. Tamor, and W. C. Vassell, "Raman fingerprinting of amorphous-carbon films", *J Appl Phys* vol. **76**, pp 3823-3830, 1994.
- [96] J. Schwan, S. Ulrich, V. Batori, H. Ehrhardt, and S. R. P. Silva, "Raman spectroscopy on amorphous carbon films", *J Appl Phys* vol. **80**, pp 440-447, 1996.
- [97] J. Kotakoski, A. V. Krasheninnikov, U. Kaiser, and J. C. Meyer, "From point defects in graphene to two-dimensional amorphous carbon", *Phys Rev Lett* vol. **106**, 2011.
- [98] M. M. Lucchese, F. Stavale, E. H. M. Ferreira, C. Vilani, M. V. O. Moutinho, R. B. Capaz, C. A. Achete, and A. Jorio, "Quantifying ion-induced defects and Raman relaxation length in graphene", *Carbon* vol. **48**, pp 1592-1597, 2010.
- [99] B. Song, G. F. Schneider, Q. Xu, G. Pandraud, C. Dekker, and H. Zandbergen, "Atomic-scale electron-beam sculpting of near-defect-free graphene nanostructures", *Nano Lett* vol. **11**, pp 2247-2250, 2011.
- [100] C. O. Girit, J. C. Meyer, R. Erni, M. D. Rossell, C. Kisielowski, L. Yang, C. H. Park, M. F. Crommie, M. L. Cohen, S. G. Louie, and A. Zettl, "Graphene at the edge: Stability and dynamics", *Science* vol. **323**, pp 1705-1708, 2009.
- [101] R. F. Egerton, P. Li, and M. Malac, "Radiation damage in the TEM and SEM", *Micron* vol. **35**, pp 399-409, 2004.
- [102] J. R. Jinschek, E. Yucelen, H. A. Calderon, and B. Freitag, "Quantitative atomic 3-D imaging of single/double sheet graphene structure", *Carbon* vol. **49**, pp 556-562, 2011.

- [103] *TEM image from Olof Bäcke, Markus Löffler, and Eva Olsson from Microscopy and Microanalysis, Chalmers University of Technology, Gothenburg, Sweden.*
- [104] *TEM images from Tim Booth and Peter Bøggild from Micro- and Nanotechnology, DTU Nanotech, Copenhagen, Denmark.*
- [105] J. Abrahamson, "The surface energies of graphite", *Carbon* vol. **11**, pp 337-362, 1973.
- [106] J. Biscoe, and B. E. Warren, "An X-Ray study of carbon black", *J Appl Phys* vol. **13**, pp 364-371, 1942.
- [107] L. Fulcheri, and Y. Schwob, "From methane to hydrogen, carbon black and water", *Int J Hydrogen Energy* vol. **20**, pp 197-202, 1995.
- [108] N. Z. Muradov, and T. N. Veziroğlu, "From hydrocarbon to hydrogen-carbon to hydrogen economy", *Int J Hydrogen Energy* vol. **30**, pp 225-237, 2005.
- [109] S. Adam, E. H. Hwang, V. M. Galitski, and S. Das Sarma, "A self-consistent theory for graphene transport", *PNAS* vol. **104**, pp 18392-18397, 2007.
- [110] J. Martin, N. Akerman, G. Ulbricht, T. Lohmann, J. H. Smet, K. Von Klitzing, and A. Yacoby, "Observation of electron-hole puddles in graphene using a scanning single-electron transistor", *Nature Phys* vol. **4**, pp 144-148, 2008.
- [111] E. A. Kim, and A. H. C. Neto, "Graphene as an electronic membrane", *Europhys Lett* vol. **84**, 2008.
- [112] J. H. Chen, C. Jang, S. Adam, M. S. Fuhrer, E. D. Williams, and M. Ishigami, "Charged-impurity scattering in graphene", *Nature Phys* vol. **4**, pp 377-381, 2008.
- [113] Y. B. Zhang, V. W. Brar, C. Girit, A. Zettl, and M. F. Crommie, "Origin of spatial charge inhomogeneity in graphene", *Nature Phys* vol. **5**, pp 722-726, 2009.
- [114] Y. P. Dan, Y. Lu, N. J. Kybert, Z. T. Luo, and A. T. C. Johnson, "Intrinsic response of graphene vapor sensors", *Nano Lett* vol. **9**, pp 1472-1475, 2009.
- [115] K. I. Bolotin, K. J. Sikes, Z. Jiang, M. Klima, G. Fudenberg, J. Hone, P. Kim, and H. L. Stormer, "Ultrahigh electron mobility in suspended graphene", *Solid State Commun* vol. **146**, pp 351-355, 2008.
- [116] X. Du, I. Skachko, A. Barker, and E. Y. Andrei, "Approaching ballistic transport in suspended graphene", *Nature Nanotech* vol. **3**, pp 491-495, 2008.
- [117] F. Chen, J. L. Xia, D. K. Ferry, and N. J. Tao, "Dielectric screening enhanced performance in graphene FET", *Nano Lett* vol. **9**, pp 2571-2574, 2009.
- [118] M. Ishigami, J. H. Chen, W. G. Cullen, M. S. Fuhrer, and E. D. Williams, "Atomic structure of graphene on SiO₂", *Nano Lett* vol. **7**, pp 1643-1648, 2007.

- [119] A. Reina, H. Son, L. Jiao, B. Fan, M. S. Dresselhaus, Z. Liu, and J. Kong, "Transferring and identification of single- and few-layer graphene on arbitrary substrates", *J Phys Chem C* vol. **112**, pp 17741-17744, 2008.
- [120] Z. Cheng, Q. Zhou, C. Wang, Q. Li, C. Wang, and Y. Fang, "Toward intrinsic graphene surfaces: A systematic study on thermal annealing and wet-chemical treatment of SiO₂-supported graphene devices", *Nano Lett* vol. **11**, pp 767-771, 2011.
- [121] A. Nourbakhsh, M. Cantoro, A. Klekachev, F. Clemente, B. Sorée, M. H. van der Veen, T. Vosch, A. Stesmans, B. Sels, and S. De Gendt, "Tuning the Fermi level of SiO₂-supported single-layer graphene by thermal annealing", *J Phys Chem C* vol. **114**, pp 6894-6900, 2010.
- [122] W. Z. Bao, F. Miao, Z. Chen, H. Zhang, W. Y. Jang, C. Dames, and C. N. Lau, "Controlled ripple texturing of suspended graphene and ultrathin graphite membranes", *Nature Nanotech* vol. **4**, pp 562-566, 2009.
- [123] J. Moser, A. Barreiro, and A. Bachtold, "Current-induced cleaning of graphene", *Appl Phys Lett* vol. **91**, p. 163513, 2007.
- [124] Z. Liu, P. Boggild, J. R. Yang, Y. Cheng, F. Grey, Y. L. Liu, L. Wang, and Q. S. Zheng, "A graphite nanoeraser", *Nanotechnology* vol. **22**, p. 265706, 2011.
- [125] R. Jalilian, L. A. Jauregui, G. Lopez, J. F. Tian, C. Roecker, M. M. Yazdanpanah, R. W. Cohn, I. Jovanovic, and Y. P. Chen, "Scanning gate microscopy on graphene: Charge inhomogeneity and extrinsic doping", *Nanotechnology* vol. **22**, p. 295705, 2011.
- [126] A. M. Goossens, V. E. Calado, A. Barreiro, K. Watanabe, T. Taniguchi, and L. M. K. Vandersypen, "Mechanical cleaning of graphene", *Appl Phys Lett* vol. **100**, p. 073110, 2012.
- [127] N. Lindvall, A. Kalabukhov, and A. Yurgens, "Cleaning graphene using atomic force microscope", *J Appl Phys* vol. **111**, pp 064904-064904, 2012.
- [128] F. Giannazzo, S. Sonde, V. Raineri, G. Patane, G. Compagnini, F. Aliotta, R. Ponterio, and E. Rimini, "Optical, morphological and spectroscopic characterization of graphene on SiO₂", *Phys Status Solidi C* vol. **7**, pp 1251-1255, 2010.
- [129] Y. Zheng, G.-X. Ni, C.-T. Toh, M.-G. Zeng, S.-T. Chen, K. Yao, and B. Özyilmaz, "Gate-controlled nonvolatile graphene-ferroelectric memory", *Appl Phys Lett* vol. **94**, pp 163505-163503, 2009.
- [130] Y. Zheng, G.-X. Ni, C.-T. Toh, C.-Y. Tan, K. Yao, and B. Özyilmaz, "Graphene field-effect transistors with ferroelectric gating", *Phys Rev Lett* vol. **105**, p. 166602, 2010.
- [131] G.-X. Ni, Y. Zheng, S. Bae, C. Y. Tan, O. Kahya, J. Wu, B. H. Hong, K. Yao, and B. Özyilmaz, "Graphene-ferroelectric hybrid structure for flexible transparent electrodes", *ACS Nano* advance online publication, 2012.
- [132] X. Hong, A. Posadas, K. Zou, C. H. Ahn, and J. Zhu, "High-mobility few-layer graphene field effect transistors fabricated on epitaxial ferroelectric gate oxides", *Phys Rev Lett* vol. **102**, p. 136808, 2009.

- [133] X. Hong, J. Hoffman, A. Posadas, K. Zou, C. H. Ahn, and J. Zhu, "Unusual resistance hysteresis in n-layer graphene field effect transistors fabricated on ferroelectric $\text{Pb}(\text{Zr}_{0.2}\text{Ti}_{0.8})\text{O}_3$ ", *Appl Phys Lett* vol. **97**, pp 033114-033113, 2010.
- [134] M. Tarasov, N. Lindvall, L. Kuzmin, and A. Yurgens, "Family of graphene-based superconducting devices", *JETP Lett* vol. **94**, pp 329-332, 2011.
- [135] L. Kuzmin, "Ultimate cold-electron bolometer with strong electrothermal feedback", *P Soc Photo-Opt Ins* vol. **5498**, pp 349-361, 2004.
- [136] Y. Nam, N. Lindvall, J. Sun, Y. W. Park, and A. Yurgens, "Graphene p-n-p junctions controlled by local gates made of naturally oxidized thin aluminium films", *Carbon* vol. **50**, pp 1987-1992, 2012.
- [137] S. Russo, J. B. Oostinga, D. Wehenkel, H. B. Heersche, S. S. Sobhani, L. M. K. Vandersypen, and A. F. Morpurgo, "Observation of Aharonov-Bohm conductance oscillations in a graphene ring", *Phys Rev B* vol. **77**, 2008.
- [138] M. Huefner, F. Molitor, A. Jacobsen, A. Pioda, C. Stampfer, K. Ensslin, and T. Ihn, "The Aharonov-Bohm effect in a side-gated graphene ring", *New J Phys* vol. **12**, 2010.
- [139] M. Huefner, F. Molitor, A. Jacobsen, A. Pioda, C. Stampfer, K. Ensslin, and T. Ihn, "Investigation of the Aharonov-Bohm effect in a gated graphene ring", *Phys Status Solidi B* vol. **246**, pp 2756-2759, 2009.
- [140] J. S. Yoo, Y. W. Park, V. Skakalova, and S. Roth, "Shubnikov-de Haas and Aharonov Bohm effects in a graphene nanoring structure", *Appl Phys Lett* vol. **96**, 2010.
- [141] P. Recher, B. Trauzettel, A. Rycerz, Y. M. Blanter, C. W. J. Beenakker, and A. F. Morpurgo, "Aharonov-Bohm effect and broken valley degeneracy in graphene rings", *Phys Rev B* vol. **76**, 2007.
- [142] A. Rycerz, "Aharonov-Bohm effect and valley polarization in nanoscopic graphene rings", *Acta Phys Pol A* vol. **115**, pp 322-325, 2009.
- [143] Y. Nam, J. S. Yoo, Y. W. Park, N. Lindvall, T. Bauch, and A. Yurgens, "The Aharonov-Bohm effect in graphene with metal mirrors", submitted to *Carbon*.